Analysis of the linear and nonlinear stability of Alfven eigenmodes and fish-bones in JET DT discharges: mode identification and shear flows generation

To cite this article: J. Varela *et al* 2025 *Nucl. Fusion* **65** 076044

OPEN ACCESS
IOP Publishing | International Atomic Energy Agency

Nuclear Fusion

Nucl. Fusion 65 (2025) 076044 (21pp)

https://doi.org/10.1088/1741-4326/ade696

Analysis of the linear and nonlinear stability of Alfven eigenmodes and fish-bones in JET DT discharges: mode identification and shear flows generation

J. Varela[1,2,*], J. Garcia[3], S. Mazzi[3], Y. Kazakov[4], Z. Stancar[5], M. Baruzzo[6,7], J. Ongena[8], D.A. Spong[9], L. Garcia[2], Y. Ghai[9], D. Zarzoso[10], J. Ortiz[2], M. Poradzinski[11], S. Sharapov[12], M. Fitzgerald[12], B. Breizman[1], F. Waelbroeck[1], S. Menmuir[12], H.J. Sun[12], D. Kos[12], A. Boboc[12], N.C. Hawkes[12], JET Contributors[a] and the EUROfusion Tokamak Exploitation team[b]

[1] Institute for Fusion Studies, Department of Physics, University of Texas at Austin, Austin, TX 78712, United States of America
[2] Universidad Carlos III de Madrid, 28911 Leganes, Madrid, Spain
[3] CEA, IRFM, F-13108 Saint Paul-lez-Durance, France
[4] Laboratory for Plasma Physics, LPP-ERM/KMS, TEC Partner, 1000 Brussels, Belgium
[5] United Kingdom Atomic Energy Authority, Culham Science Centre, Abingdon, United Kingdom of Great Britain and Northern Ireland
[6] Consorzio RFX, Corso Stati Uniti 4, Padova, Italy
[7] ENEA for EUROfusion, Via E. Fermi 45, 00044 Frascati (Roma), Italy
[8] Plasma Physics Laboratory—Royal Military Academy, Renaissancelaan 30, 1000 Brussels, Belgium
[9] Oak Ridge National Laboratory, Oak Ridge, TN 37831-8071, United States of America
[10] Aix Marseille Univ, CNRS, Centrale Med, M2P2 Marseille, France
[11] Institute of Plasma Physics and Laser Microfusion, Hery str. 23, 01-497 Warsaw, Poland
[12] UKAEA, Culham Science Centre, Abingdon, Oxfordshire OX14 3DB, United Kingdom of Great Britain and Northern Ireland

E-mail: jacobo.rodriguez@austin.utexas.edu

Received 6 March 2025, revised 12 June 2025
Accepted for publication 20 June 2025
Published 27 June 2025

Abstract

The plasma in future nuclear fusion reactors will be heated by neutral beam injectors (NBIs) and high frequency electromagnetic waves as well as fusion born alpha particles. Energetic particles (EPs), with energies up to two orders of magnitude larger than the thermal plasma, can trigger EP driven modes and induce harmful EP losses, reducing the plasma heating efficiency

[a] See Maggi *et al* 2024 (https://doi.org/10.1088/1741-4326/ad3e16) for JET Contributors.
[b] See Joffrin *et al* 2024 (https://doi.org/10.1088/1741-4326/ad2be4) for the EUROfusion Tokamak Exploitation Team.
[*] Author to whom any correspondence should be addressed.

and the economical viability of the reactor. The present study is dedicated to analyze the Alfven Eigenmode (AE) activity in JET D–T discharges, the closest experiment to reactor-like operation performed until now. There, EP driven modes are induced by the combined effect of tangential NBIs and ion cyclotron resonance heating (ICRH) driven EP. Linear and nonlinear simulations are performed with the gyro-fluid FAR3d code to analyze the AE activity observed in the discharge 99896. The linear simulations reproduce the unstable $n = 3$ to 5 toroidal AEs (TAE) at the inner plasma region observed in the experiment, triggered by highly energetic passing deuterium populations injected by the tangential NBIs, further accelerated by the effect of the ICRH up to 1 MeV. In addition, fish-bones triggered by energetic trapped hydrogen induced by the ICRH are also reproduced. On the other hand, the alpha particles density is too small to destabilize AEs in the experiment. Nonetheless, increasing artificially the alpha density by one order of magnitude, an $n = 1$ beta induced AE can be destabilized in the inner plasma region. Nonlinear simulations indicate the generation of zonal structures during the AE/fish-bone saturation phase. TAE and fish-bones causes a rather weak increase of the passing D and trapped H EP (around 2%), respectively. Shear flows and zonal currents are generated during the saturation of TAE and fish-bones. Nonlinear simulations performed for D–T and pure deuterium thermal plasma indicate AE/fish-bone activity is weaker and shear flows are less intense in the pure deuterium case, trends consistent with the experimental observations that also indicates a deterioration of the thermal plasma confinement. Therefore, both numerical studies and experimental evidence indicate the generation of shear flows by AE/fish-bones could be connected with an improvement of the thermal plasma confinement.

Keywords: tokamak, JET, MHD, AE, fish-bones and shear flows

(Some figures may appear in colour only in the online journal)

1. Introduction

Nuclear fusion reactors require an efficient plasma heating to reduce the operational requirement and maximize their economical viability. Unfortunately, energetic particles (EPs) generated by external actuators applied to heat the plasma as neutral beam injectors (NBIs) and ion cyclotron resonance heating (ICRF) can induce EP driven instabilities, leading to an enhancement of EP turbulent losses before thermalization [1–5]. EP driven instabilities also affect the confinement of alpha particles, called to be the main heating mechanism of reactor relevant plasma [6, 7]. Experiments in TFTR, JT-60U, DIIID, EAST, ASDEX and KSTAR tokamaks [8–13] as well as LHD, W7-AS, W7-X, TJII and Heliotron J stellarators [14–18] show a decrease of the device performance if EP driven instabilities are triggered, enhancing EP diffusive loses and an inefficient plasma heating.

EP driven instabilities are triggered if the EP drift, bounce or transit frequencies resonate with the shear Alfven waves [2], leading to the destabilization of Alfvén eigenmodes (AE) in the gaps of the shear Alfvén continua [19, 20]. In addition, EP modes (EPM) can be unstable inside the continuum if the EP destabilizing effect is large enough to exceed the continuum damping [21, 22].

Unstable AEs are observed routinely in the Joint European Torus (JET) discharges [23–28]. In particular, toroidal AE (TAE) resulting of coupled m with $m+1$ waves (m is the poloidal mode number) [29, 30], ellipticity AE (EAE) caused by coupled m with $m+2$ waves [31], global AEs (GAE) observed when there is an extreme in the Alfvén continua [32] and reversed-shear AEs (RSAE) due to local maxima/minima in the safety factor q profile [33] are measured. In addition, EPMs seeded by current gradient driven modes called fish-bones are also observed [34].

Different numerical models were applied to analyze the AE stability in JET plasma, in particular TAEs [35–38]. Nonlinear simulations performed to study shear flows induced during the AEs and Fish-bones saturation phase may cause a reduction of the plasma turbulence level, leading to an improvement of the thermal plasma confinement [39–46]. In fact, there is experimental evidence of shear flows generation by AE/EPM in LHD, EAST and JET experiments that may affect the thermal plasma confinement [47, 48].

A new experimental campaign using deuterium–tritium (D–T) plasmas [49] was performed in JET tokamak [50] dedicated to the exploration of reactor relevant Physics [51]. In particular, configurations with ITER-like properties are analyzed, showing high electron heating, low input torque, an alpha particle population and rather large AE activity [52]. The experiments reveal plasma with good energy confinement and stability, showing reduced energy losses for the electron and core ion transports, particularly if EP driven instabilities are observed [52].

JET plasma is heated by two NBI boxes equipped with eight positive beam injector [53, 54] operating at 125 kV providing up to 34 MW. In addition, an ICRH system with four antennas can inject up to 4–5MW in the frequency band raging 23–56 kHz [55, 56]. The combination of NBI and ICRH heating in

-DT plasma using H minority lead to an improved D–T reactivity for moderate input power configurations [57–60].

The present study is dedicated to analyze the linear and nonlinear stability of AEs and fish-bones in the JET DT discharge 99896, a 50%–50% D–T plasma with 1% of hydrogen used as a minority wave resonator for ICRF heating. The analysis aim is providing physics reasons of the improved thermal energy confinement in the presence of fast ions instabilities [52], connecting the shear flow enhancement calculated in nonlinear simulations and improved thermal plasma confinement observed in the experiments with a stronger AE activity. Linear simulations are performed to identify the type of instabilities observed in the experiments, calculating the resonances leading to AEs and fish-bone destabilization. On that aim, parametric studies are performed with respect to the density and energy of several EP populations in the plasma, including in the study passing D EP injected by the NBI, trapped H EP generated by the ICRH and alpha particle born in the fusion reactions. The correct identification of the resonances implies reproducing the same frequency range, mode number and radial location of the measured instability. Nonlinear simulations provide qualitative information of the AE/fish-bones saturation phase, in particular the induced EP transport and energy transfers towards the thermal plasma leading to the generation of zonal structures.

The FAR3d code calculates the plasma stability by solving a set of reduced nonlinear resistive MHD equations couple with moments of the gyrokinetic equation, particularly the energetic ion density and parallel velocity [61–64], in a three dimensional equilibria generated by the VMEC code [65]. Linear wave-particle resonance effects are introduced in the model by Landau closure relations (Landau damping/growth).

This paper is organized as follows. First, the instabilities measured in the experiment are described section 2. Next, the numerical model, equilibria and main thermal plasma and EP profiles are indicated section 3. The results of the linear simulations are shown in section 4. Nonlinear simulations outcome is discussed in section 5. The EP transport calculated in the nonlinear simulations for each EP species is discussed in section 6. The effect of the EP energy and thermal plasma species on the AE stability and shear flow intensity is introduced in section 7. Finally, the conclusions of this paper are presented in section 8.

2. Instabilities measured in the discharge 99896

This section is dedicated to introduce the instabilities measured in the discharge 99896. Figure 1, panel (*a*), shows four different phases along the discharge with respect to the plasma heating pattern. First, the plasma is heated only by a deuterium beam. From $t = 7$ s, ICRF is also injected in the plasma. Next, at $t = 9$ s, the deuterium beam is switched by a tritium beam. Finally, at $t = 10.5$ s, the tritium beam stops and the plasma is only heated using ICRF. Panel (*b*) indicates the presence of instabilities in the plasma at different frequency ranges based on the Mirnov coils data. No instabilities are observed in the discharge phase with only deuterium beam although several instabilities appear as soon as the ICRH is injected. In particular, the instabilities in the frequency range below 50 kHz are identified as neoclassical tearing modes (NTMs), around 15 kHz, fish-bones at 25 kHz and RSAE at 20 kHz. NTM is a pressure driven MHD instability linked to the bootstrap current [66, 67]. Higher frequency modes are also observed from 150 to 190 kHz identified as TAEs. In addition, there is a faint activity between 220 and 240 kHz that could be included in the frequency range of the EAEs. It should be noted that instabilities frequency sweeping, particularly high frequency modes, is caused by variations of the thermal plasma density and q profile along the discharge. The triangular wave in the background is caused by the active TAE antenna diagnostic, not part of the current investigation [68] although introduced in the appendix regarding the analysis of the modes damping rates in the simulation and the experiment. Once the tritium beam replaces the deuterium beam, instabilities show an up-shift of the frequency around 10 kHz, new TAEs are triggered between 120 to 150 kHz, NTM are strongly destabilized although fish-bones get weaker. At the end of the discharge, once the plasma is only heated by ICRH, NTM and fish-bones are weaker showing a fast frequency down-shift while the high frequency modes experience a fast up-shift. Panel (*c*) indicates high frequency instabilities are $n = 1$ to 5 TAEs (n is the toroidal mode number), including $n = 1$ and 2 TAEs propagating in both direction (positive and negative toroidal mode number). The strongest instability is the $n = 4$ TAE. Panel (*d*) shows a rather strong $n = 3$ NTM and the $n = 6$ NTM overtone around 30 kHz as well as fish-bones triggered by $n = 1$ toroidal mode family. In addition, $n = 0$ zonal structures are measured at frequency ranges below 2 kHz.

In the following, the analysis will be focus in the discharge phase with deuterium beam and ICRH. Consequently, the coupling between passing D injected in the plasma by the NBI and ICRH is included in the simulations, described as a bump tail of the passing D EP population.

3. Equations and numerical scheme

The analysis is performed with the gyro-fluid code FAR3d [69] including the destabilizing effect of the EPs [70] and parallel momentum thermal plasma response [71]. The EP distribution function is assumed Maxwellian [41, 72].

The linear stability is calculated using the code Eigenvalue solver to identifying sub-dominant modes, that is to say, the simulations identify all the possible channels the free energy have to trigger instabilities. Nonlinear simulation are performed using the initial value solver.

FAR3d code participated in bench-marking studies showing similar results compared to gyro-kinetic and hybrid codes [73]. FAR3d code was applied to model the MHD activity in LHD [74–78], DIII-D [79–83], TJ-II [18, 84–86] and Heliotron J [17, 87, 88] plasma, showing a reasonable

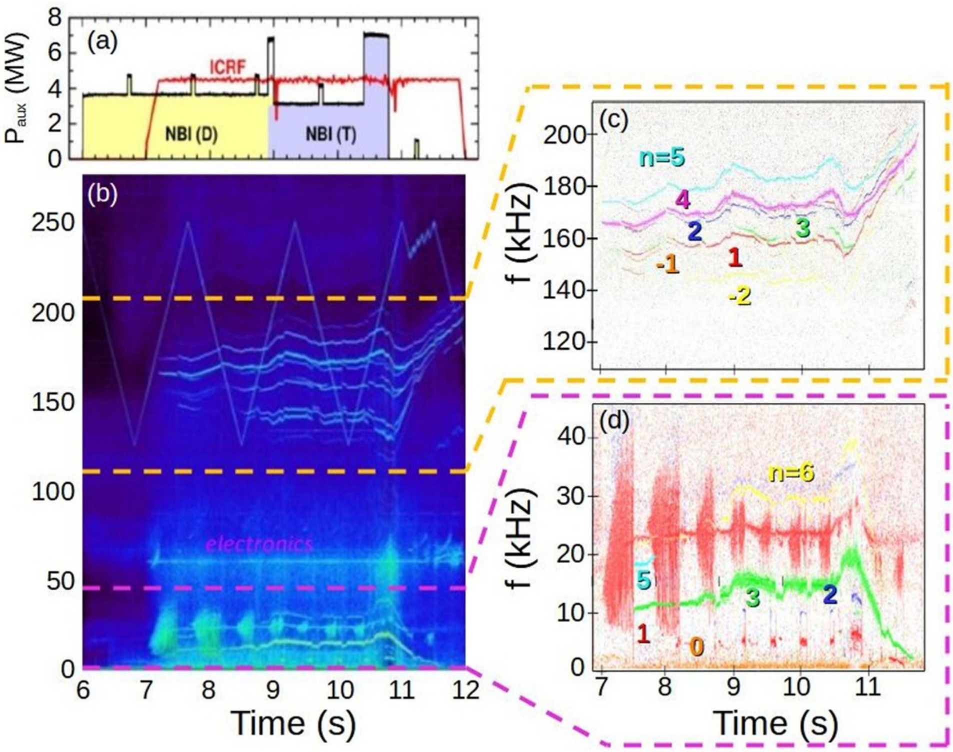

Figure 1. Discharge 99896. Time evolution of (*a*) NBI and ICRH power injection, (*b*) spectrogram of the magnetic diagnostics. Instability toroidal mode number for (*c*) high and (*d*) low frequency instabilities. The frequency range of high (low) frequency modes is indicated by orange (purple) horizontal dashed lines.

agreement. In addition, nonlinear studies were dedicated to analyze sawtooth-like and internal collapse events in LHD plasma [89–92] as well as the AE saturation in DIII-D plasma [45, 46]. FAR3d code was applied to analyze the AE stability in plasma with multiple EP populations for LHD, DIII-D, ITER and CFETR [93–95], to predict the MHD stability of devices as JT-60SA, CFQS and QPS [72, 96, 97] and the analysis of the AE/EPM saturation in LHD plasma [98, 99].

3.1. Equilibrium properties

The discharge 99896 has a D–T concentration of 50%D–50%T with 1% of Hydrogen used as a minority wave resonator for ICRF heating, a toroidal current $I_{\mathrm{p}} = 1.9$ MA, magnetic field $B_{\mathrm{T}} = 2.8$ T, and $q_{95} = 4.5$. The plasma is heated using ICRF power up to 4.5 MW and NBI power of 3.5 MW. The plasma is in a newly discovered I-mode like DT regime [52], there are no ELMs and a normalized thermal plasma β of 1.2%.

The TRANSP suite of modeling codes is used to calculate the plasma equilibrium as well as the thermal plasma and EP profiles [100]. TRANSP model is coupled with external heating modules NUBEAM (NBI) [101] and TORIC (ICRF) [102], and prepared with the OMFIT integrated modeling platform [103]. The fitting of thermal electron temperature and density as well as thermal ion temperature is performed using high resolution Thomson scattering (HRTS) [104] and charge exchange recombination spectroscopy (CXRS) [105]. An EFIT equilibrium of the discharge 99896 at $t = 8.57$ s is calculated and translated to a VMEC equilibrium including the effect of the energetic ions pressure in the force balance [65, 106]. The q profile is validated using as markers $q = 4/3$ and $1/1$ rational surfaces, linked to the toroidal model number of NTMs and fish-bones (obtained from the toroidal array of Mirnov coils), identifying the radial location by measuring the perturbed electron temperature from Electron Cyclotron Emission (ECE) diagnostic and the modes frequency derived from the Mirnov coils to the Doppler-shifted plasma rotation (with toroidal plasma rotation obtained from charge exchange diagnostic). The radial location of RSAEs and TAEs is measured using Soft x-ray cameras, interferometry and reflectometry diagnostics.

Figure 2 shows the main thermal and EP profiles of the model. Panel (*a*) indicates a region of negative magnetic shear nearby the magnetic axis, around $r/a < 0.15$, and the $q = 1$ rational surface is located at the plasma core. Panels (*b*) and (*c*) show the thermal ion/electron density and temperature indicating the formation of a pedestal although no edge localized mode (ELM) activity is observed in the experiment [107]. The radial location of the density profile gradient for passing D EPs injected by the NBI and trapped H EPs generated by the ICRH, panels (*d*) and (*e*) respectively, are observed in the inner-middle plasma region. Thus, AEs/EPMs triggered by these EP populations must be located at $r/a < 0.65$. On the other hand, the gradient of the alpha particle density is located nearby the magnetic axis, around $r/a = 0.0 - 0.25$.

The destabilizing effect of the different EP populations is evaluated performing a set of parametric studies with respect

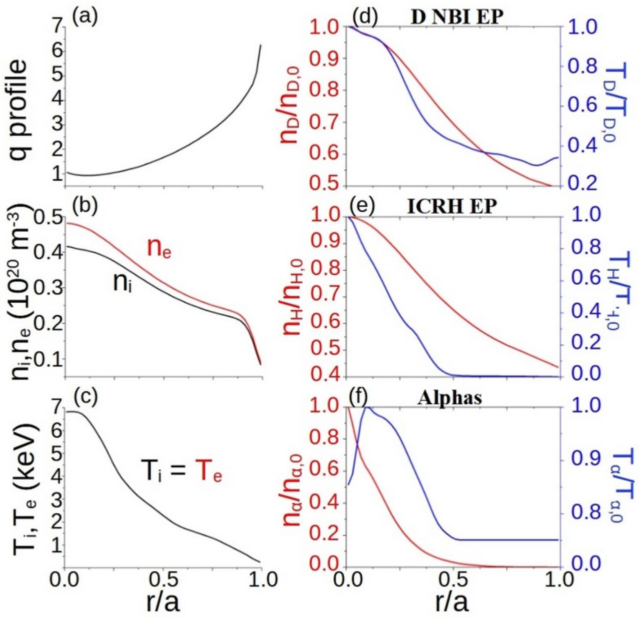

Figure 2. Main profiles in the discharge 99896. (*a*) *q* profile, (*b*) thermal electron and ion density, (*c*) thermal electron and ion temperature, (*d*) passing D density and energy, (*e*) trapped H density and energy, (*f*) alpha particle density and energy. Here, $r/a = \sqrt{\Psi}$ with Ψ the toroidal flux.

to the EP energy (T_{f}) and β (β_{ep}). On that aim, the EP density and energy profiles are up or down scaled. The passing D resonance is evaluated for the energies 96, 250, 500, 750 and 1000 keV and EP β of 0.21 and 0.52. The passing D resonance for 96 keV corresponds to the averaged energy of a Maxwellian EP distribution fitting the slowing down distribution in a plasma purely heated by the NBI. Passing D resonances from 250 to 1000 keV correspond to the case of a plasma heated by the combination of NBI and ICRH injection, that is to say, the destabilizing effect caused by bump tails of passing D further accelerated by the ICRH [108]. Trapped H resonance is analyzed for the energies 26, 100, 250, 500 and 1000 keV and EP β of 0.01, 0.1 and 0.3. In addition, the H trapping level is evaluated with respect to the EP bounce frequency (ω_{b}) and bounce distance (r_{b}). Here, r_{b} and ω_{b} represent the bounce length and frequency of the guiding center of a trapped EP trajectory in the ρ—θ plane (for further information of the EP trapped model please see [64]). Small r_{b} values analyze resonances causes by deeply trapped EPs. The bounding frequency is fixed using the approximated value calculated from the equation (13) in [109], 215 kHz, although different bounding distances are tested, 0.1, 0.01 and 0.001 m (smaller r_{b} indicates a deeply H trapping). Regarding the alpha particles, resonances generated by populations with energies of 500, 1000, 1500, 2000 and 3000 keV for EP β of 0.0045, 0.045 and 0.225 are analyzed. It should be noted that the Maxwellian distribution function assumed for the passing D and trapped H are an approximation of the real EP slowing down distribution in the experiment, consequently deviations between simulation results and experiment observations may exist because the EP resonance are drive are not accurately reproduced. Nevertheless, performing parametric scans with respect to the EP β and energy provide a better approach by identifying the optimal configuration that better reproduce the experimental observations.

Table 1. Toroidal (n) and poloidal (m) modes in the simulations.

n	m
0	[0, 24]
1	[1, 4]
2	[2, 8]
3	[3, 12]
4	[4, 16]
5	[5, 20]
6	[6, 24]

3.2. Simulation parameters

Table 1 shows the toroidal (n) and poloidal (m) modes included in the simulations, including all the resonance between the magnetic axis and $r/a < 0.9$. The number of point of the radial grid is 400 for the nonlinear simulations and 200 for the linear simulations.

The moments of the gyro-kinetic equation breaks the MHD symmetry thus both parties must be included for all the dynamic variables. The magnetic Lundquist number is $S = 10^7$ and the diffusivity is $D_i = 10^{-5}$ (normalized to $v_{A0}^2 \tau_{A0}$ with $\tau_{A0} = 4.9 \cdot 10^{-7}$ s the Alfven time at the magnetic axis and $v_{A0} = 5.8 \cdot 10^6$ m s^{-1} the Alfven speed at the magnetic axis). The effect of the thermal ion and EP finite Larmor radius (FLR) as well as electron—ion Landau damping are analyzed in the linear and nonlinear simulations. For further information see the appendix. The compressibility factor in the simulations is $\Gamma = 1$. Further information about the damping effect implementation in the code are found in the [96]. Neoclassical effects are not included in the model thus the analysis of NTM is out of the scope of the study. The plasma resistivity is calculated using the profile of the thermal electron temperature scaled to the magnetic Lundquist number.

The nonlinear simulation of the passing D EP are performed using an EP energy of 1000 keV and EP $\beta = 0.3$. Trapped H nonlinear simulation is done using an EP energy of 1000 eV, EP $\beta = 0.4$, bounding distance of 0.0008 m and bounding frequency of 215 kHz. For the alpha particles, the EP energy is 1160 keV and EP $\beta = 0.05$.

4. Linear stability

The aim of this section is to identify the EP species responsible for the AE/EPM activity observed in the experiment. Thus, AE/EPM linear stability analysis is performed considering the destabilizing effect of passing D, trapped H and alpha particles. Different EP resonances are explored with respect to the EP energy and β (as well as trapped EP bounding distances for the case of the trapped H). The identification of the best parametric set approximating the real resonance should provide a reasonable agreement between simulation

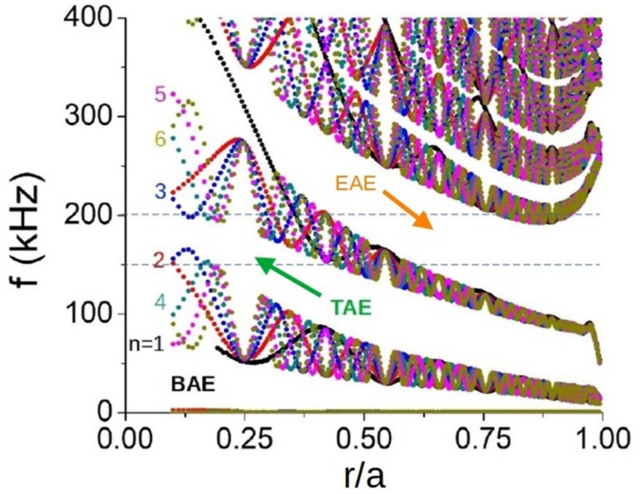

Figure 3. Alfven gaps of the toroidal families $n = 1$ to 6 in the discharge 99896 at $t = 8.57$ s. Green (orange) arrow indicate the radial location of the TAE (EAE) gap consistent with the frequency range of the AE activity in the experiment (horizontal dashed lines).

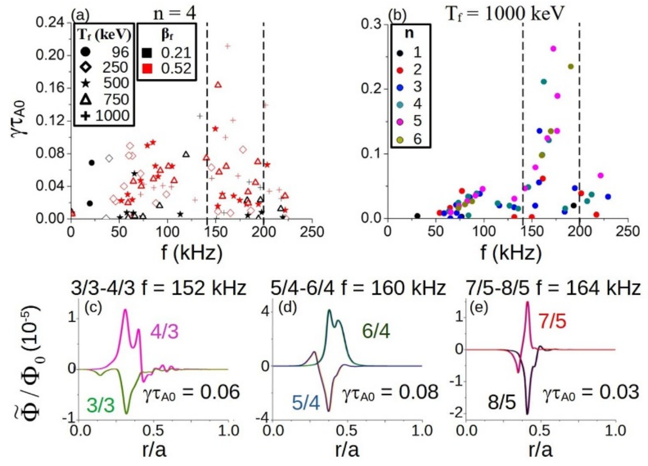

Figure 4. (*a*) Growth rate and frequency of $n = 4$ AEs destabilized by passing D populations in simulations with different EP energy and β (no FLR). (*b*) Growth rate and frequency of $n = 1$ to 6 AEs if EP energy is 1000 keV and EP $\beta = 0.52$ (no FLR). Vertical dashed lines indicate the frequency range of the AEs observed in the experiment. Eigenfunction, frequency and growth rate of the dominant AEs if the EP energy is 1000 keV and EP $\beta = 0.52$ in simulations including thermal ion and EP FLR damping effects (*c*) $3/3 - 4/3$ TAE, (*d*) $5/4 - 6/4$ TAE and (*e*) $7/5 - 8/5$ TAE.

and observations with respect to the AE/EPM frequency, radial location and instability mode number. In addition, the parametric analysis provides information of the critical EP β required to destabilize the modes (EP density) and information about the EP resonance along the slowing down process (EP energy).

Figure 3 indicates the Alfven gaps of the toroidal families $n = 1$ to 6 calculated by the code Stellgap including the effect of the acoustic wave coupling [110]. The AE activity measured in the frequency range between 150 to 200 kHz (horizontal dashed lines) could be TAEs destabilized in the inner-middle plasma region or EAEs unstable in the middle-outer plasma. Nevertheless, JET diagnostics revealed AEs are located around $r/a = 0.25$–0.45, thus the unstable modes should be TAEs. This result provides a guideline for the interpretation of the following stability analysis.

4.1. Passing deuterium EP injected by the NBI

Figure 4, panel (*a*), shows unstable $n = 4$ AEs in the frequency range of the experiment if the EP energy is $\leqslant 500$ keV for EP $\beta = 0.21$ although $\leqslant 250$ keV for EP $\beta = 0.52$. That means passing D EP injected by the NBI (96 keV) cannot trigger AEs, consistent with the absence of AE activity during the discharge phase only heated by NBI. Consequently, only a bump tail of EP with energies $\geqslant 250$ generated during the discharge phase combining NBI and ICRH heating can trigger AEs. In addition, simulations for EP energies of 250 keV or higher and EP β of 0.52, the modes calculated with the largest growth rates show a frequency consistent with the observations, in the range of 150–200 kHz. Panel (*b*) indicates that all $n = 1$ to $n = 6$ AEs have the fastest growing modes in the frequency range of the experiment if the EP energy is 1000 keV and EP $\beta = 0.52$. Thus, the resonance induced by a bump tail of passing D with energies around 1000 keV (also if the EP energy is 750keV, data not shown) may explain the experimental observations. It should be noted that the simulations shown in panels (*a*) and (*b*) do not include FLR effects, leading to the destabilization of EAEs in the middle plasma region, around $r/a = 0.6$. This result is inconsistent with the observations that locate the AEs inwards, around $r/a = 0.25$–0.45. On the other hand, simulations including FLR damping effects cause a strong stabilization on the EAEs and the fastest growing modes are TAEs located in the inner plasma. Panels (*c*)–(*e*) show $3/3 - 4/3$, $5/4 - 6/4$ and $7/5 - 8/5$ TAEs localized at $r/a = 0.35$–0.4 with frequencies between 152 and 164 kHz. The mode with the highest growth rate is the $n = 4$ TAE, consistent with the observations. The $n = 1$, 2 and 6 TAEs are stable in the simulations although $n = 1$ and 2 perturbations in the TAE frequency range are observed in the experiment. Such $n = 1$ and 2 modes can be caused by the nonlinear interaction of $n = 3$, 4 and 5 TAEs and the $n = 3$ NTM [52], thus the linear simulations showing $n = 1$ and 2 TAEs are stable do not contradict the experimental observations. Nevertheless, it is also possible the EP distribution function and radial profiles uncertainty may lead to an inaccurate description of the EP drive and identification of $n = 1$ and 2 TAEs activity. The frequency of the TAEs calculated is around 10 kHz smaller compared to the experiment, discrepancy that can be explained by the lack of the equilibrium toroidal rotation in the simulations (Doppler effect).

Summarizing, the parametric analysis indicates AEs measured in the frequency range of 150–200 could be triggered by a bump tail of passing D with energies $\geqslant 750$ keV, generated by the synergy of NBI and ICRH heating sources, in particular

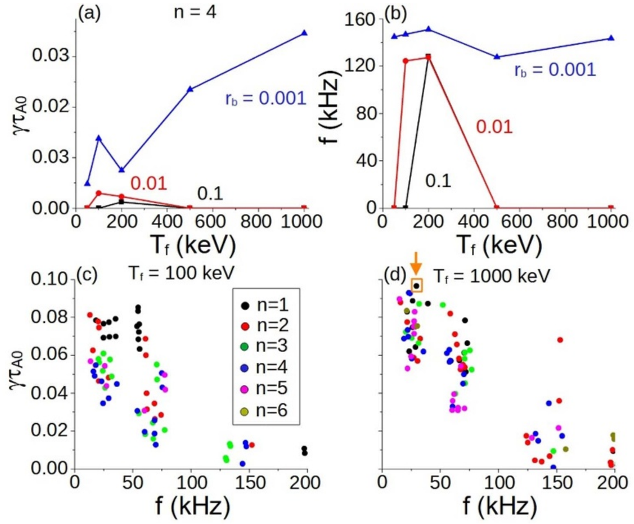

Figure 5. (*a*) Growth rate and (*b*) frequency of $n = 4$ AE/EPM destabilized by trapped H populations with different EP energies and bounce distances if $\beta = 0.3$ and the dominant perturbation is an EP driven mode (no FLR). Growth rate and frequency of $n = 1$ to 6 AE/EPM destabilized by trapped H populations if $\beta = 0.3$ (no FLR) for an EP energy of (*c*) 100 and (*d*) 1000 keV. Orange square and arrow indicate the mode plotted in figure 6.

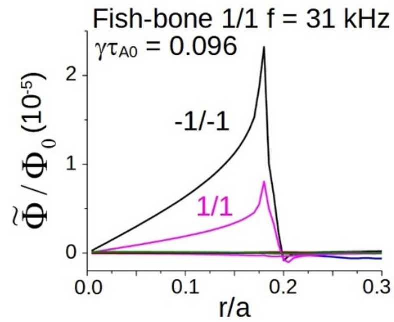

Figure 6. Eigenfunction of the fish-bone triggered by trapped H if $\beta = 0.3$ and EP energy is 100 keV (orange square in figure 5, panel (*c*)).

passing D EP injected by the NBI further accelerated by the ICRH.

4.2. Trapped H EP generated by the ICRH

Figure 5, panels (*a*) and (*b*), show that deeply trapped H EP ($r_b = 0.001$) with energies $\geqslant 26$ keV and EP $\beta = 0.3$ can destabilize $n = 4$ AEs with frequencies above 120 kHz. Weakly trapped H EP ($r_b = 0.01$ and 0.1) destabilize AEs showing a lower growth rate and frequencies above 120 kHz if the EP energy is 100–250 kHz. It should be noted that panels (*a*) and (*b*) only include the simulation result for dominant EP driven mode. This is the case for all the EP energies analyzed for deeply trapped H EP, showing approximately a linear trend between mode frequency and EP energy. This is not the case for weakly trapped H EP simulations because the dominant instability changes from an EP driven mode to an internal kink above a given threshold of the EP energy. For this reason the linear trend between mode frequency and EP energy is not observed. Panels (*c*) and (*d*) indicate AEs/EPMs with the largest growth rate are located at frequencies around 60 kHz if the EP energy is 100 keV although they are around 30 kHz if the EP energy is 1000 keV. Consequently, resonances linked to trapped H mainly destabilize low frequency modes and should not be the main driver of AEs at frequencies above 150 kHz. Figure 6 shows the eigenfunction of the $n = 1$ perturbation with the largest growth rate and frequency below 50 kHz that corresponds to a fish-bone with a frequency of 31 kHz triggered in the inner plasma region (indicated by an orange square in figure 5(*d*)).

In summary, the parametric analysis indicates the trapped H mainly destabilize low frequency modes, in particular fish-bones. Thus, trapped H cannot be the main driver of the instabilities observed in frequency ranges above 150 kHz. On the other hand, trapped H resonance may cause the fish-bones observed in the frequency range of 25–35 kHz.

4.3. Fusion born alpha particle

Figure 7, panels (*a*) and (*b*), indicate AEs are not triggered by alpha particles if EP $\beta = 0.0045$ for any of the EP energy tested. The simulations with EP $\beta = 0.0045$ represent the experimental conditions that show a rather low content of alpha particles. EP β must be increased by one order of magnitude, simulations with 0.045 for all the EP energy tested, to destabilize $n = 1$ AEs in the frequency range between 60 and 80 kHz. Nevertheless, $n = 4$ AEs are stable and EP β must be further increased to be destabilized (simulations with 0.225). Panel (*c*) shows the destabilization of a $1/1$ BAE nearby the magnetic axis with a frequency of 77 kHz in the simulation for EP $\beta = 0.045$ and EP energy of 3000 keV.

The analysis results suggest alpha particles population is too small to trigger AEs in the experiment. EP β of the simulation must be increased at least on order of magnitude larger compared to the real alpha particle density to destabilize $1/1$ BAE located nearby the magnetic axis.

5. Nonlinear stability

Nonlinear simulations are performed to analyze the saturation phase of AEs and fish-bones triggered by passing D EP, trapped H EP and alpha particles. Study of the AEs and fish-bone saturation phase provides information on the induced EP transport, energy exchange between other modes and thermal plasma, deformation of the flux surfaces as well as the generation of zonal structures. The analysis for each EP species is performed independently. It should be noted that nonlinear studies using a gyro-fluid model must be considered as a first step of the AE/EPM saturation analysis and comparisons with the experimental observations must be done qualitatively. In addition, important limitations to measure the saturated amplitude of AE/EPM exist given the high level of noise in diagnostics dedicated to measure the thermal plasma perturbations induced by the AE/EPM using ECE data. In particular, for the discharge analyzed, no information of the saturated

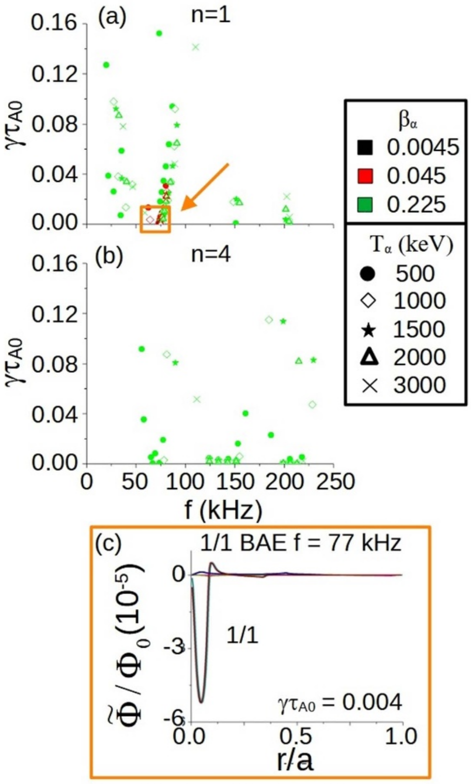

Figure 7. Growth rate and frequency of (*a*) $n = 1$ and (*b*) 4 AEs destabilized by alpha particles for different EP energies and β (no FLR). The orange square and arrow indicate the mode plotted in the panel (*c*).

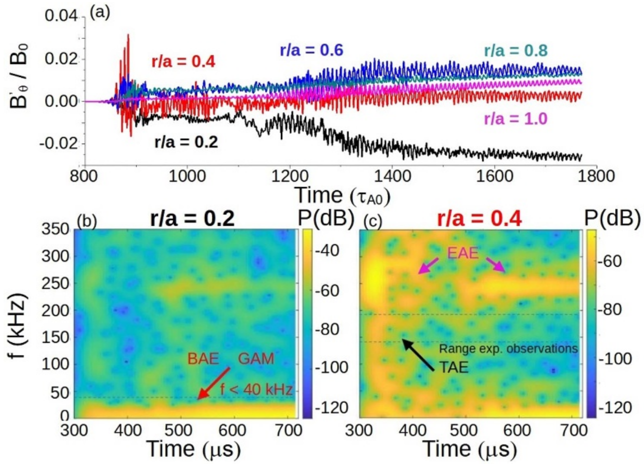

Figure 8. Passing D EP nonlinear simulation. (*a*) Normalized value of the poloidal magnetic field perturbation at different plasma radius ($r/a = 0.2$, black, 0.4, red, 0.6, blue, 0.8, cyan, 1.0, pink). Spectrogram of the normalized poloidal magnetic field perturbation at (*b*) $r/a = 0.2$ and (*c*) $r/a = 0.4$. The red arrow and dashed line in panel (*b*) indicate the frequency range of the most unstable modes. The black arrow and dashed line in panel (*c*) indicate the frequency range of the unstable modes consistent with the high frequency modes observed in the experiment. The pink arrow indicates modes in the frequency range of the EAEs.

amplitude of fish-bones and TAEs is available to compare with the simulation results.

5.1. Saturation of TAEs

Figure 8, panel (*a*), indicates TAEs triggered in the inner-middle plasma region ($r/a = 0.2$–0.6) during the linear phase of the simulation (until $t = 850\tau_{A0}$ with τ_{A0} the Alfven time at the magnetic axis). Once the simulation enters in the initial saturation phase (from $t = 850$ to $1100\tau_{A0}$) there is an enhancement of the plasma perturbation, particularly nearby the magnetic axis ($r/a = 0.2$), further enhanced from $t = 1100\tau_{A0}$ (late saturate phase). Panel (*b*) shows the plasma perturbation nearby the magnetic axis is linked to low frequency modes, below 40 kHz, the frequency range of beta induced AE (BAE) or geodesic acoustic modes (GAMs) [111–113]. Panel (*c*) indicates a larger frequency spreading for the perturbations at $r/a = 0.4$, consequence of the strong nonlinear interaction between different unstable modes. Modes in the TAE frequency range are destabilized during the simulation linear and saturation phases (150–200 kHz). In addition, modes in the frequency range of the EAEs (250 kHz) are triggered during the simulation linear and late saturation phases.

Figure 9, panels (*a*)–(*c*), indicate two local maxima of the thermal plasma kinetic (KE) and magnetic (ME) energy as well as the EP perturbation energy (EPE) during the initial and late saturation phases. EPE is defined as $E_{\text{ep}} = n_{\text{ep}} v_{||,\text{ep}}^2$ with n_{ep} the EP density perturbation and $v_{||,\text{ep}}$ the EP parallel velocity perturbation, KE as $E_k = n(v_r^2 + v_\theta^2)$ with n the equilibrium thermal plasma density and $v_r v_\theta$ the radial and poloidal components of the thermal plasma velocity perturbation, ME as $E_k = B_r^2 + B_\theta^2$ with $B_r B_\theta$ the radial and poloidal components of the magnetic field perturbation. It should be mentioned that EPE is a third-order perturbation although KE and ME are second order perturbations, thus EP and thermal plasma energy cannot be directly compared and the analysis only provides qualitative information of the thermal plasma distortion induced by the unstable AEs. The first energy maximum is linked to the transition from the linear to the saturation phase ($t = 850\tau_{A0}$), indicating $n = 3$ toroidal family causes the strongest plasma relaxation and the most energetic modes, in particular the poloidal modes $m = 5$ to 8. The local maximum of EPE is correlated with local maxima of KE and ME, indicating part of the AE energy is channel towards the thermal plasma, invested in the generation of shear flows and the perturbation of the plasma flux surfaces as well as the induction of zonal currents and the distortion of the magnetic surfaces. The $n = 3$ modes stabilize along the initial saturation phase observed as the fast decay of the EPE energy between $t = 850$ to $1050\tau_{A0}$ followed by a decrease of the KE and ME. The second maximum is observed during the late saturation phase, at $t = 1150\tau_{A0}$ for the EPE although at $t = 1300\tau_{A0}$ for KE and ME. Firstly, $n = 1$ modes are destabilized around $t = 1100\tau_{A0}$, particularly the poloidal modes $m = 1$ to 3, sharing energy with the thermal plasma that shows the largest distortion $t = 100\tau_{A0}$ later with respect to maximum perturbation induced by the $n = 1$ modes. Consequently, AE stability features in initial and late saturation phase are different.

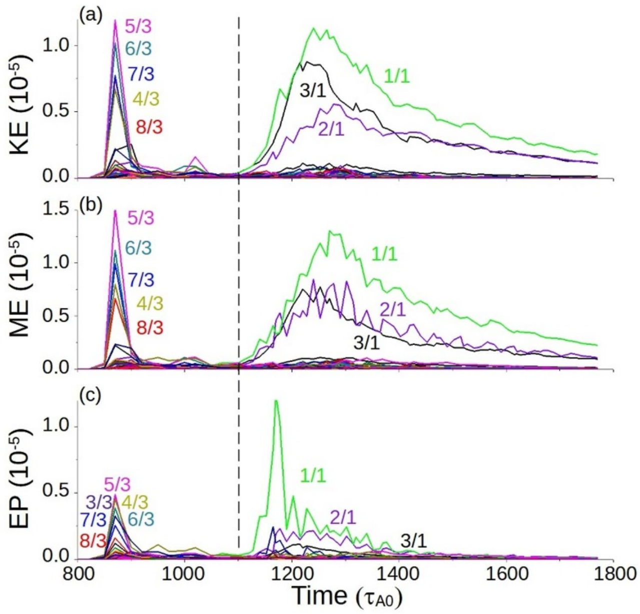

Figure 9. Passing D nonlinear simulation. Volume integrated normalized (*a*) kinetic, (*b*) magnetic and (*c*) Alfven eigenmodes energy. The dashed vertical line indicates the transition time from initial to late saturation phases.

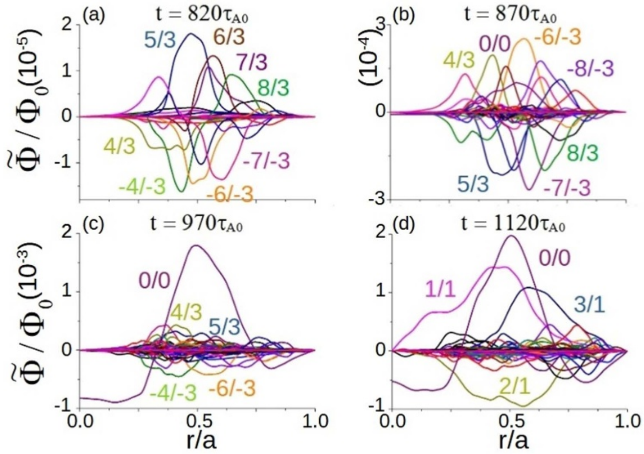

Figure 10. Passing D nonlinear simulation. Electrostatic potential eigenfunction at (*a*) $t = 820\tau_{A0}$, (*b*) $t = 870\tau_{A0}$, (*c*) $t = 970\tau_{A0}$ and (*d*) $t = 1120\tau_{A0}$.

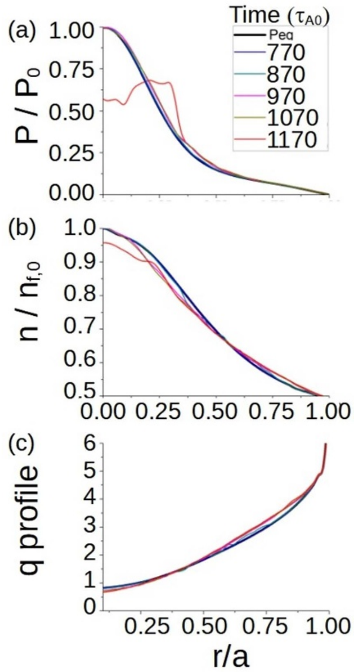

Figure 11. Passing D nonlinear simulation. Evolution of the (*a*) thermal plasma pressure, (*b*) EP density and (*c*) q profile.

Figure 10, panel (*a*), indicates the destabilization of a $4/3-5/3$ TAE in the inner-middle plasma region and a $6/3-8/3$ EAE in the middle-outer plasma region during the linear phase ($t = 820\tau_{A0}$). TAE and EAE saturate, panel (*b*), transferring part of their energy towards the thermal plasma causing the destabilization of the $0/0$ mode ($t = 870\tau_{A0}$). Along the saturation phase TAE and EAE stabilize, panel (*c*), although the mode $0/0$ is further destabilized showing the largest amplitude, pointing out the perturbation induced on the thermal plasma by the AEs remains active after the AE stabilization ($t = 970\tau_{A0}$). Once the simulation enters in the late saturation phase, a global $1/1-1/3$ EAE is triggered showing a large radial width covering the main part of the plasma. AEs eigenfunction analysis confirms the transition in the AE activity comparing initial and late saturation phases.

Figure 11, panel (*a*), indicates a rather weak effect of AEs on the thermal pressure profile during linear and initial saturation phases, perturbation mainly localized in the inner-middle plasma region where the unstable TAEs are sited. On the other hand, as soon as the global $1/1-1/3$ EAE is triggered at the beginning of the late saturation phase, a large decrease of the thermal plasma pressure is observed in the inner plasma region. This result may indicate the global $1/1-1/3$ EAE induces a stronger perturbation on the thermal plasma compared to the localized TAEs. Panel (*b*) shows a drop of the EP density profile in the inner-middle plasma region linked to AEs triggered during linear and initial saturation phases, as well as an slightly increase of the profile at the outer plasma region linked to the radial redistribution of passing D EP. The rather small variation of the EP density profile may indicate EP transport and radial redistribution induced by TAEs is small. There is a larger decrease of the EP density profile nearby the magnetic axis during the late saturation phase, pointing out the destabilization of the global $1/1-1/3$ EAE causes a stronger EP transport. Panel (*c*) shows an excursions of the q profile associated with zonal currents induced by the AEs during the saturation phase, a small decrease nearby the magnetic axis although an increase in the middle-outer plasma region.

Figure 12, panels (*a*)–(*c*), indicate the destabilization of the $4/3-5/3$ TAE mixed with the $6/3-8/3$ EAE in the inner-middle plasma region at $t = 820\tau_{A0}$, AEs saturation and $0/0$ destabilization in the inner plasma region at $t = 970\tau_{A0}$ as well as the further destabilization of $0/0$ mode in the inner plasma as soon as the global $1/1-1/3$ EAE is triggered at $t = 1170\tau_{A0}$. Panels (*d*)–(*f*) show the generation of zonal

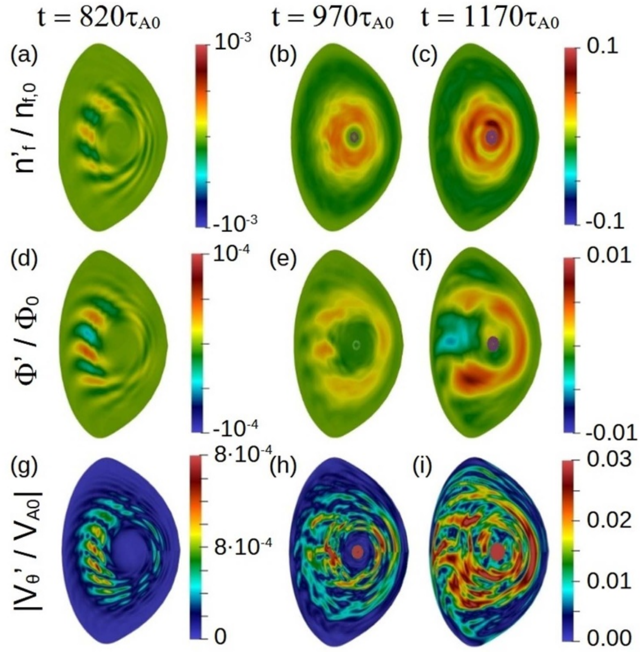

Figure 12. Passing D nonlinear simulation. Evolution of the poloidal contour of the normalized perturbation of the EP density (*a*)–(*c*), electrostatic potential (*d*)–(*f*) and module of the poloidal thermal plasma flow (*g*)–(*i*).

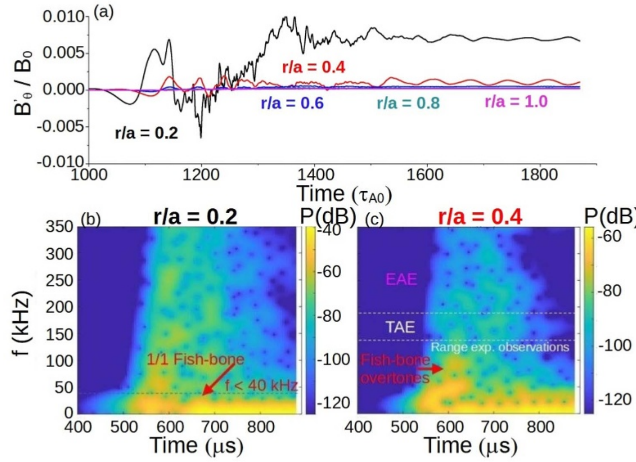

Figure 13. Trapped H nonlinear simulation. (*a*) Normalized value of the poloidal magnetic field perturbation at different plasma radius ($r/a = 0.2$, black, 0.4, red, 0.6, blue, 0.8, cyan, 1.0, pink). Spectrogram of the normalized value of the poloidal magnetic field perturbation at (*b*) $r/a = 0.2$ and (*c*) $r/a = 0.4$. The red arrow in panels (*b*) and (*c*) indicate the frequency range of the most unstable modes. The red dashed line in panel (*c*) indicate the frequency range of the unstable modes consistent with the low frequency instabilities observed in the experiment. White dashed lines in the panel (*d*) indicate the frequency range of the high frequency instabilities observed in the experiments.

structures by $4/3-5/3$ TAE and $6/3-8/3$ EAE during the initial saturation phase in the inner-middle plasma region, displaced to the inner plasma as the saturation phase evolves, further enhanced once the global $1/1-1/3$ EAE appears. Panels (*g*)–(*i*) indicate the generation of shear flows first in the inner-middle plasma region where $4/3-5/3$ TAE and $6/3-8/3$ EAE are triggered, further enhanced along the saturation phase particularly after global $1/1-1/3$ EAE destabilization.

In summary, the simulation shows two different phases with respect to the AE activity. First, a $4/3-5/3$ TAE mixed with the $6/3-8/3$ EAE are triggered in the inner-middle plasma region, leading to a rather weak effect on the EP transport an radial redistribution. These modes are located in the frequency range between 150 and 250 kHZ, consistent with the experiment. Nevertheless, EAE activity is very weak in the experiment, pointing out the simulations exaggerate the destabilizing effect of the EP on the EAEs. This discrepancy can be explained by the thermal ion and EP FLR effects used in the simulations, not large enough to efficiently damp EAEs. In addition, the rather large uncertainty of the thermal plasma and EP profiles affect the radial location and frequency range of the continuum gaps and the plasma region where the AEs are more unstable, thus the configuration analyzed could be more favorable to the destabilization of the EAEs compared to the real experiment. AEs saturate channeling part of the energy towards the thermal plasma leading to the generation of zonal structure (the mode $0/0$ is destabilized), in particular shear flows. The shear flows may affect the plasma turbulence and confinement while the zonal current can modify locally the magnetic field topology. The initial saturation phase provides a reasonable description of the experimental observations although the late saturation phase reproduces a configuration showing a transition from the soft MHD limit (local plasma relaxation) to the hard MHD limit (global plasma relaxation) not observed in the experiment. A global $1/1-1/3$ EAE is triggered due to the perturbation induced by the AEs on the thermal plasma during the initial saturation phase, that is to say, the saturation of the $4/3-5/3$ TAE and $6/3-8/3$ EAE cause a modification on the thermal and EP profiles leading to a further destabilization of the $n = 1$ EAE. The destabilization of the global $1/1-1/3$ EAE strongly affects the thermal pressure profile in the inner plasma, indicating a strong energy channeling from the EAE to the thermal plasma strongly modifying the flux surface in the inner plasma region. In addition, the global EAE enhances the EP transport and shear flows. That means, hard MHD limit transition should be avoided to prevent an increment of the EP transport and strong perturbations in the thermal plasma.

5.2. Saturation of fish-bones

Figure 13, panel (*a*), indicates a fish-bone destabilized in the inner plasma ($r/a = 0.2$) during the linear phase of the simulation (until $t = 1050\tau_{A0}$). The inner plasma region is further destabilized during the saturation phase showing an enhancement of the perturbation at $r/a = 0.2$–0.4. Panel (*b*) shows the destabilization of low frequency modes below 40 kHz identified as fish-bones (in combination with zonal structures) nearby the magnetic axis. Panel (*c*) indicates the frequency range of the perturbations extend up to 100 kHz at $r/a = 0.4$, particularly at the beginning of the saturation phase linked to the destabilization of fish-bone overtones.

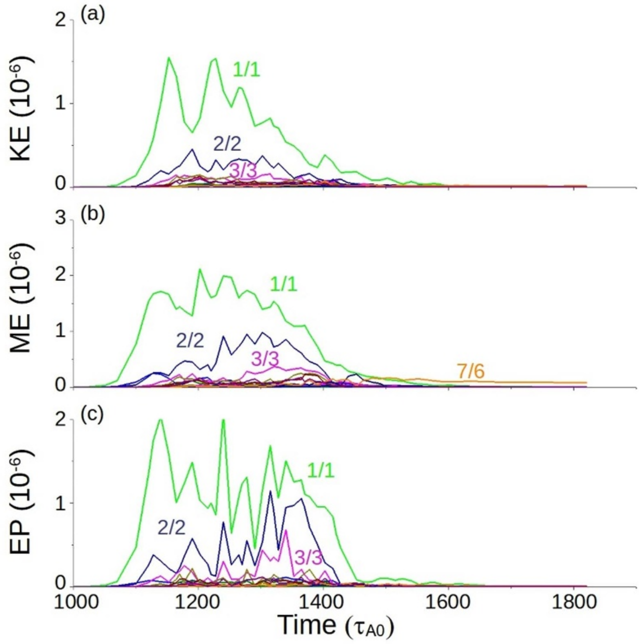

Figure 14. Trapped H nonlinear simulation. Volume integrated normalized (*a*) kinetic, (*b*) magnetic and (*c*) Alfven eigenmodes energy.

Figure 14, panels (*a*)–(*c*), show several maxima of the EPE correlated with KE and ME maxima. Once the simulation enters in the saturation phase there is a large increase of $1/1$ mode energy, followed by the modes $2/2$ and $3/3$, overtones of the fish-bone. Overtones are unstable because a fraction of the fish-bone energy is transferred to other toroidal mode families. In addition, fish-bone and overtones channel their energy to the thermal plasma leading to the generation of zonal structures, the deformation of the plasma flux surfaces and local modification of the magnetic field topology. Successive local maximum of the EPE may suggest the destabilization of short period fish-bone oscillations. Fish-bone and overtones saturate after $t = 400\tau_{A0}$ once the energy transfer to the thermal plasma ends.

Figure 15, panel (*a*), shows the eigenfunction of the fish-bone triggered nearby the magnetic axis during the linear phase of the simulation ($t = 1020\tau_{A0}$). Panel (*b*) indicates the fish-bone as well as $2/2$ and $3/3$ overtones eigenfunction during the saturation phase. The fish-bone covers all the inner plasma although overtones are located closer to the middle plasma region, around $r/a = 0.25 - 0.35$. The energy channeling from fish-bones and overtones towards the thermal plasma causes the destabilization of the $0/0$ mode, showing the largest amplitude.

Figure 16, panel (*a*), indicates fish-bones and overtones cause 40% decrease of the thermal plasma pressure in the inner plasma region, pointing out a large distortion of the flux surfaces. It should be noted that the large drop of the pressure profile is correlated with the destabilization of fish-bone overtones, thus the resonance overlapping between perturbations may lead to a transition to the hard MHD limit in the inner plasma and the partial collapse of the thermal plasma pressure.

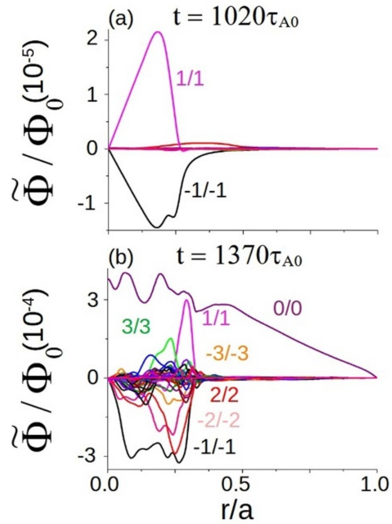

Figure 15. Trapped H nonlinear simulation. Electrostatic potential eigenfunction at (*a*) $t = 1020\tau_{A0}$ and (*b*) $t = 1270\tau_{A0}$.

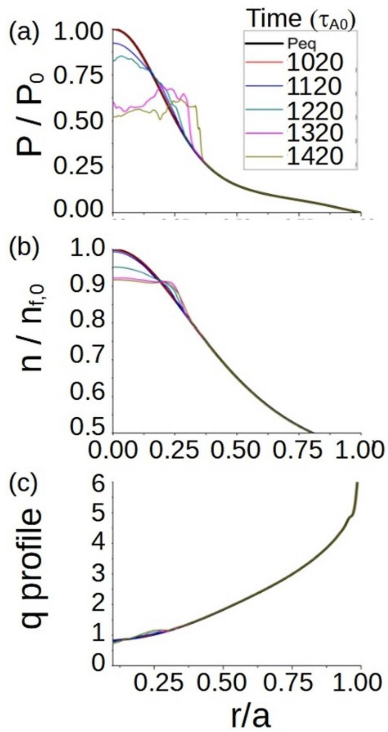

Figure 16. Trapped H nonlinear simulation. Evolution of the (*a*) thermal plasma pressure, (*b*) EP density and (*c*) *q* profile.

Panel (*b*) indicates there is a flattening of the EP density profile nearby the magnetic axis induced by fish-bone and overtones, thus EP transport is increased and there is a redistribution of the EPs in the inner plasma region. Panel (*c*) shows the rather weak effect of the zonal currents on the *q* profile, indicating only a small excursion in the inner plasma region.

Figure 17, panels (*a*) and (*b*), indicate the $1/1$ fish-bone perturbation nearby the magnetic axis at the beginning of the saturation phase ($t = 1120\tau_{A0}$). The perturbation is further

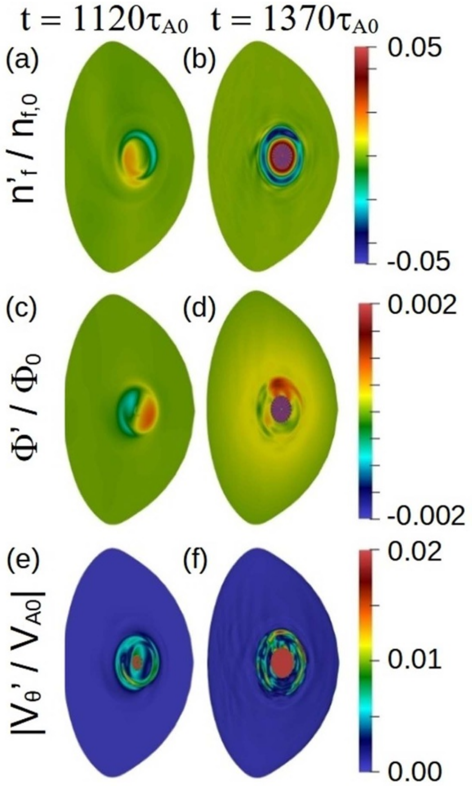

Figure 17. Trapped H nonlinear simulation. Evolution of the poloidal contour of the normalized perturbation of the EP density (*a*) and (*b*), electrostatic potential (*c*) and (*d*) and module of the poloidal thermal plasma flow (*e*) and (*f*).

enhanced along the simulation showing a more complex structure at the middle plasma region due to the destabilization of the overtones ($t = 1370\tau_{A0}$). Panels (*c*) and (*d*) indicate the presence of zonal structures linked to fish-bone and overtones generating shear flows in the inner plasma region, as can be seen in panels (*e*) and (*f*).

To conclude, fish-bone and overtones saturation lead to an energy transfer towards the thermal plasma inducing large distortions of the flux surfaces and the generation of shear flows in the inner plasma. Overlapping between fish-bone and overtones may cause a transition to the hard MHD regime in the inner plasma leading to a partial thermal plasma pressure collapse. In addition, fish-bones lead to an increment of the EP transport and redistribution in the inner plasma region. On the other hand, induced zonal currents and q profile excursions are rather small.

5.3. Saturation of alpha particle driven AE

This study is dedicated to analyze an hypothetical scenario based on a JET discharge extrapolated to study a reactor relevant configuration with an alpha particle population large enough to trigger AEs, exploring the alpha particle transport induced during the AEs saturation phase. Figure 18, panel (*a*), shows the destabilization of a BAE nearby the magnetic axis ($r/a = 0.2$) during the linear phase of the simulation (until

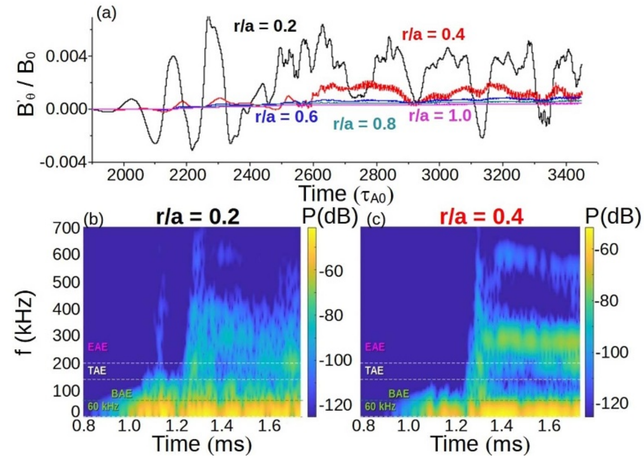

Figure 18. Alpha particle nonlinear simulation. (*a*) Normalized value of the poloidal magnetic field perturbation at different plasma radius ($r/a = 0.2$, black, 0.4, red, 0.6, blue, 0.8, cyan, 1.0, pink). Spectrogram of the normalized value of the poloidal magnetic field perturbation at (*b*) $r/a = 0.2$ and (*c*) $r/a = 0.4$.

$t = 2050\tau_{A0}$) performed with an EP $\beta = 0.045$, 10 times larger than the experimental value. An oscillating perturbation pattern is observed during the saturation phase, firstly located nearby the magnetic axis although also observed in the inner plasma region ($r/a = 0.4$) from $t = 2600\tau_{A0}$. Panels (*b*) and (*c*) indicate the most unstable modes are triggered in the frequency range below 50 kHz, covering all the inner plasma. In addition, there is a weak activity in the frequency range of TAE and EAE as well as faint modes up to 600 kHz.

Figure 19, panel (*c*), indicates the destabilization of a 1/1 BAE at $t = 2050\tau_{A0}$ as well as overtones 2/2, 3/3 and 4/4 at $t = 2500\tau_{A0}$ destabilized due to the nonlinear energy channeling from $n = 1$ to higher n modes. Panels (*a*)–(*c*) indicate a correlation between the first local maxima of EPE, KE and ME during the saturation phase, around $t = 2200\tau_{A0}$, denoting the perturbation induced by the BAE on the thermal plasma due to energy channeling. From $t = 2200$ to $t = 2350\tau_{A0}$ EPE energy decreases indicating the 1/1 BAE is weakened although ME and KE energy remain almost unchanged. From $t = 2350\tau_{A0}$, 1/1 BAE is further destabilized showing an EPE maximum 2 times larger compared with the first maximum at $t = 2500\tau_{A0}$. It should be noted that the local maxima of KE and ME are observed $t = 50\tau_{A0}$ before the local maximum of the EPE, indicating the energy transfer from the 1/1 BAE and overtones towards the thermal plasma is reinforced along the saturation phase.

Figure 20, panel (*a*), show the eigenfunction of the 1/1 BAE triggered nearby the magnetic axis in the simulation linear phase ($t = 2050\tau_{A0}$). Panel (*b*) indicates the eigenfunction at the first EPE maxima ($t = 2200\tau_{A0}$) along the saturation phase, showing an increase of 1/1 BAE amplitude and the destabilization of the 0/0 mode in the inner plasma region. Panel (*c*) shows the destabilization of 2/2, 3/3 and 4/4 BAEs also located at the inner plasma region as well as a further increase of 1/1 BAE and 0/0 mode amplitude.

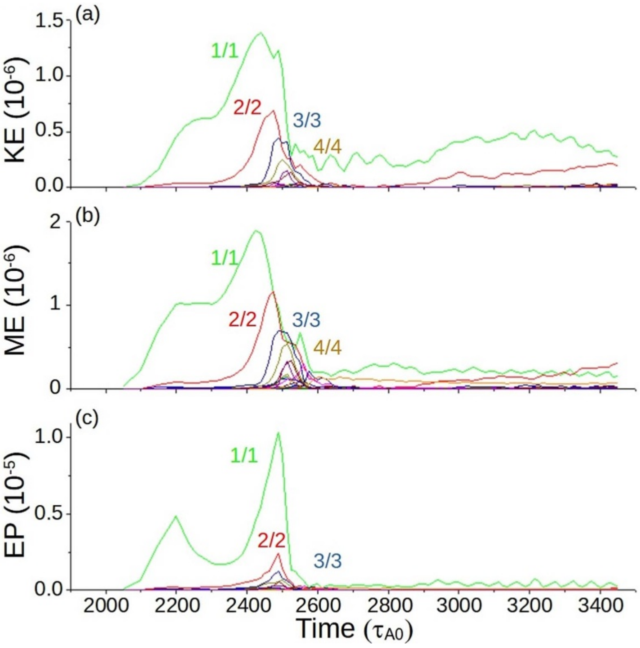

Figure 19. Alpha particles nonlinear simulation. Volume integrated normalized (*a*) kinetic, (*b*) magnetic and (*c*) Alfven eigenmodes energy.

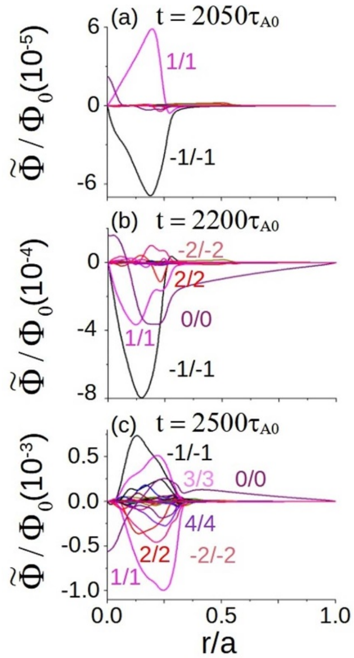

Figure 20. Alpha particles nonlinear simulation. Electrostatic potential eigenfunction at (*a*) $t = 2050\tau_{A0}$, (*b*) $t = 2200\tau_{A0}$ and (*c*) $t = 2500\tau_{A0}$.

Figure 21, panel (*a*), indicates a rather small effect of $1/1$ BAE on the thermal pressure at the beginning of the saturation phase, from $t = 2100$ to $t = 2300\tau_{A0}$, leading to a pressure profile decrease at the magnetic axis smaller than 5%. On the other hand, there is a drop of the thermal pressure down by 40% at $t = 2500\tau_{A0}$ correlated with the destabilization of $1/1$ BAE overtones, pointing out there is a hard MHD transition in

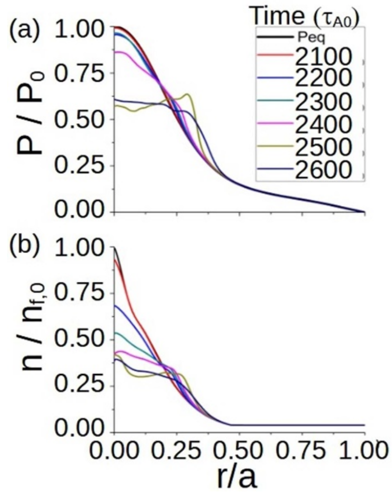

Figure 21. Alpha particles nonlinear simulation. Evolution of the (*a*) thermal plasma pressure and (*b*) EP density.

the inner plasma caused by resonance overlapping. Panel (*b*) shows an enhancement of the alpha particle transport linked to the $1/1$ BAE leading to 15% decrease of the alpha particle density at the magnetic axis (red line, $t = 2100\tau_{A0}$). Once the overtones are also unstable (blue line, $t = 2200\tau_{A0}$), EP transport is further increased inducing a 30% alpha particle density drop. No information about zonal currents effects on the q profile is discussed because no excursions of the safety factor profile are observed along the simulation.

Figure 22, panels (*a*)–(*c*), indicate a $1/1$ perturbation linked to the $1/1$ BAE nearby the magnetic axis triggered during the simulation linear phase ($t = 2050\tau_{A0}$), further enhanced along the saturation phase ($t = 2200\tau_{A0}$). The destabilization of $1/1$ BAE overtones leads to propagation of the perturbation towards the middle plasma region as the saturation phase advance. Likewise, shear flows get stronger along the simulation as can be observed in panels (*g*)–(*i*).

Concluding, the saturation of $1/1$ BAE and overtones triggered by the alpha particles in an hypothetical scenario with an EP β one order of magnitude higher than the experimental values, causes a strong distortion of the flux surfaces in the inner plasma linked to the resonance overlapping and the transition to the hard MHD limit. Shear flows are firstly induced by the energy transfer from $1/1$ BAE towards the thermal plasma, also channeled to higher n modes leading to overtones destabilization and a further enhancement of the shear flows. In addition, large alpha particle losses can be induced by BAEs.

6. EP transport induced by TAEs, fish-bones and BAEs

This section is dedicated to analyze the EP transport induced by AEs and fish-bones for each EP species analyzed. Figure 23 indicates a rather weak passing D and trapped H EP transport caused by TAE and fish-bones, respectively. Trapped H EP and passing D EP losses are below 1% at the end of the

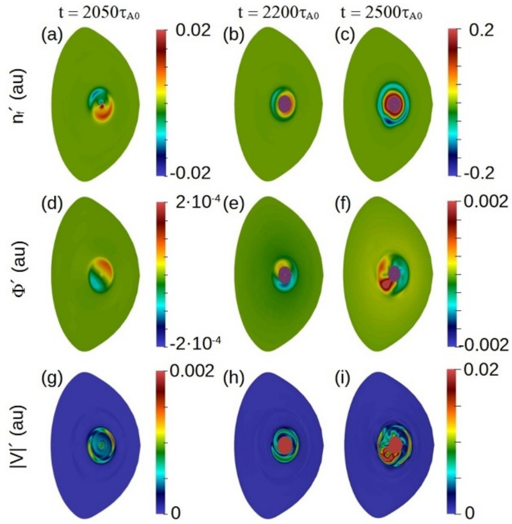

Figure 22. Trapped H nonlinear simulation. Evolution of the poloidal contour of the normalized perturbation of the EP density (*a*)–(*c*), electrostatic potential (*d*) and (*f*) and module of the poloidal thermal plasma flow (*h*) and (*i*).

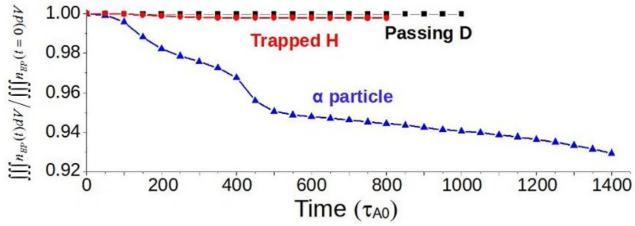

Figure 23. Volume integral of the EP density along the simulation normalized to the volume integral of the equilibrium EP density for the passing D EP (black line), trapped H EP (red line) and alpha particles (blue line) for the nonlinear simulations analyzed in the previous section. Time is re-normalized with respect to the graphs in previous section, setting $t = 0$ as the time once the saturation phase begins in each simulation.

simulation, thus the small transport induced by fish-bones and TAEs in the simulations show similar trends with respect to the experiment, measurements indicating that the pitch angle characteristics of the high energy particle losses do not correspond to the typical ICRH accelerated ions but rather to alpha particles. The opposite scenario is observed in the hypothetical scenario for alpha particles, because $1/1$ BAE and overtones cause losses around 6% at the end of the simulation. First, $1/1$ BAE destabilization induces around 3% of alpha particle losses, further enhanced up to 6% once the overtones are also unstable and Hard MHD limit is reached. Consequently, the destabilization of BAEs may have a significant impact on the alpha particle confinement leading to the impairment of future reactor performance. On the contrary, fish-bones and TAEs do not cause important losses of trapped H and passing D EP, respectively, thus controlled destabilization of these modes may provide an useful method to improve the thermal plasma confinement by reducing the plasma turbulence due to the generation of shear flows. This result may explain the good thermal plasma confinement in the discharge analyzed, as discussed in [52]. Nevertheless, as it is discussed in the follow-up article dedicated to nonlinear simulation including multiple EP species for the same D–T JET discharge, fish-bones may have an effect on the confinement of alpha particles which would limit the efficiency of EP driven modes for alpha power enhancement.

7. AE activity and shear flows: consequences on thermal plasma confinement

The aim of this section is to analyze the connection between AE activity and shear flows intensity, identifying trends in the nonlinear simulation that may correlate enhanced shear flows with improved thermal plasma confinement, the case of the experimental observations. Gyrokinetic and hybrid simulations of bulk plasma turbulence in the presence of EP show a reduction of the radial heat flux linked to the generation of shear flows nearby saturating EP driven modes (together with kinetic nonlinearity of the resonant EPs) [114–117], pointing out that substantial velocity shear may have a stabilizing effect on the ITG modes that are responsible for heat transport in the plasma core. A set of four nonlinear simulations are performed for passing D and trapped H EPs modifying EP energy and thermal plasma species with respect to the reference cases discussed in the previous section. In particular, two simulations are performed reducing the EP energy from 1000 to 500 keV, leading to a weakening of the EP resonance and a decrease of TAE/fish-bones intensity (see figures 4 and 5), and another two simulations replacing the D–T thermal plasma by pure deuterium and keeping the same EP energy (only the Alfven velocity is modified due to the lower mass ratio of the pure deuterium plasma). Experiments performed in pure deuterium plasma show weaker AE activity and a deterioration of the thermal plasma confinement compared to D–T discharges [52], thus the new simulations may show weaker AE/fish-bone activity and shear flows in case shear flows and thermal plasma confinement are correlated.

Figure 24 indicates the amplitude of the poloidal magnetic field perturbation is smaller compared to the reference cases for both passing D and trapped H nonlinear simulations reducing the EP energy or using a pure deuterium thermal plasma (please see figures 8 and 13). New passing D simulations show a decrease of 30% compared to the reference case, TAE amplitude is 50% smaller and the most unstable modes are $9/6 - 10/6$ (pure thermal deuterium plasma) and $8/5 - 9/5$ (500 kev) TAEs (data not shown). In addition, EPE energy decrease around 50% (data not shown). On the other hand, the perturbation in the new trapped H simulations only decreases by 10% with respect to the reference case, fish-bone amplitude reduces around 15% and EPE energy is 10% smaller (data not shown). Consequently, these results indicate TAE/fish-bone activity is smaller in the new nonlinear simulations as

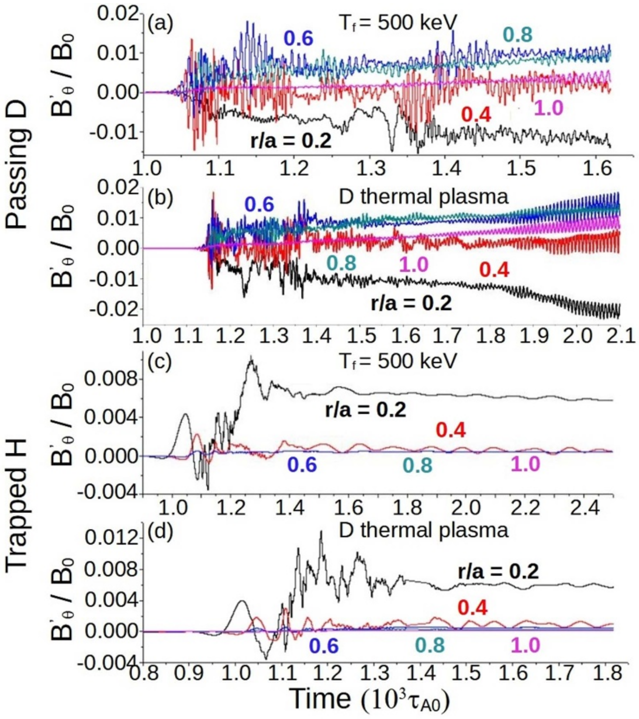

Figure 24. Normalized value of the poloidal magnetic field perturbation at different plasma radius ($r/a = 0.2$, black, 0.4, red, 0.6, blue, 0.8, cyan, 1.0, pink) for (*a*) passing D with 500 keV for DT thermal plasma, (*b*) passing D with 1000 keV for D thermal plasma, (*c*) trapped H with 500 keV for DT thermal plasma, (*d*) trapped H with 1000 keV for D thermal plasma.

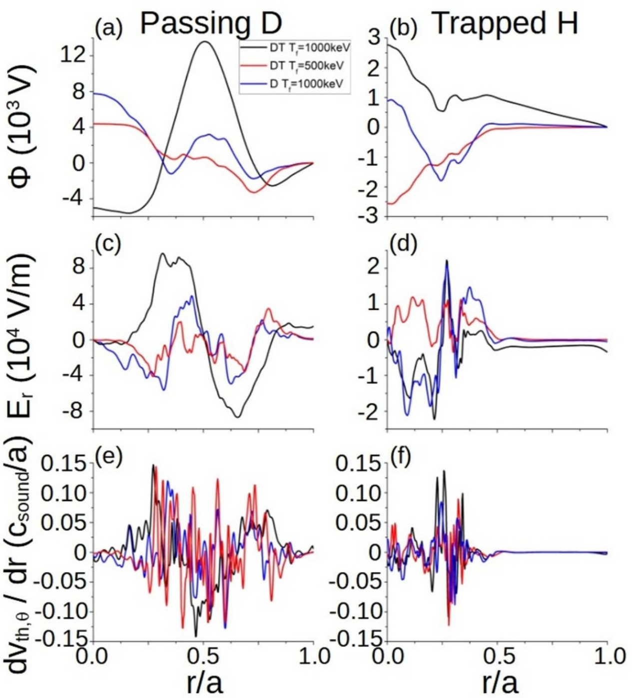

Figure 25. Radial electrostatic potential in simulations with different EP energy and thermal plasma species in nonlinear simulation for (*a*) passing D and (*b*) trapped H EP. Radial electric field in simulations with different EP energy and thermal plasma species in nonlinear simulation for (*c*) passing D and (*d*) trapped H EP. Radial derivative of the thermal plasma poloidal velocity perturbation for (*e*) passing D and (*f*) trapped H EP. The frequency is normalized to the thermal plasma velocity and the minor radius. DT plasma for an EP energy of 1000 keV, black line, DT plasma for an EP energy of 500 keV, red line, D plasma for an EP energy of 1000 keV, blue line.

expected from the linear study results, although the trend is more remarkable for TAEs.

Figure 25, panels (*a*) and (*b*), indicate TAE/fish-bones lead to weaker zonal structures in the new nonlinear simulations, particularly for the passing D, showing a decrease of the electrostatic perturbation in the inner-middle plasma region around 70%. The reduction of the zonal structures is less evident in the trapped H cases with a decrease around 10% at the inner plasma in the new simulation. Panels (*c*) and (*d*) may indicate shear flows are stronger in the passing D reference case because the radial electric field induced during the TAE saturation is more than two times stronger compared to the new simulations. On the other hand, trapped H reference case shows an electric field is only slightly larger compared to the new simulations. It should be noted the electrostatic potential and radial electric field generated during TAEs saturation are four times larger compared to the fish-bones, pointing out the shear flows induced by the TAEs are stronger compared to the fish-bones. This trend is confirmed in panels (*e*) and (*f*), indicating a larger shear of the poloidal component of the thermal plasma velocity by the TAEs compared to the fish-bones. In addition, radial electric field and poloidal flow shear generated by the TAEs reach the maximum in the middle plasma region although it is observed in the inner plasma region for the fish-bones. Gyrokinetic simulations predict the stabilization of ion temperature gradient (ITG) modes, that main source of the ion scale turbulence in fusion devices, if shear flows are strong enough by increasing the critical temperature gradient threshold for the ITG destabilization [118, 119]. The stabilizing effect of shear flows on ITG can be analyzed in the first approximation by calculating the shear generated in the simulations normalized to the sound speed and the minor radius. If the values obtained are close to the unit, ITG can be strongly suppressed by the shear flows [120]. We observe in the simulation the amplitude of the shear values oscillate for the DT case with 1000 keV between 0.15 and $-0.15c_{\mathrm{sound}}/a$ for the TAEs, and 0.13 to $-0.12c_{\mathrm{sound}}/a$ for the fish-bone. Consequently, the shear flows in the simulation can have a important effect on the ITG stability. Nevertheless, further analysis are required to verify these results, performing nonlinear simulations including the saturation of both EP driven modes and ITGs, a topic out of the scope of the present analysis.

In summary, weaker TAE/fish-bone activity is linked to less intense shear flows and zonal currents. In addition, shear flows induced by TAEs are stronger compared to fish-bones, particularly in the middle plasma region. The generation of shear flows by TAEs in the middle plasma and by fish-bones in the inner plasma region may explain the improved thermal plasma confinement observed in the experiments, leading to a reduction of the plasma turbulence and anomalous transport comparing D–T and pure D discharges.

8. Conclusions and discussion

The simulations discussed in the article aim to be a first step in the validation of gyro-fluid models applied to the study of D–T plasmas. This task is mandatory for developing reliable tools dedicated to study the heating efficiency of reactor relevant plasma, particularly the prediction of the stability of EP driven modes and induced EP fluxes in devices as ITER and DEMO.

D–T JET discharge 99896 shows AE activity in the frequency range of 150 to 190 kHz as well as low frequency modes identified as fish-bones, NTM and RSAE below 50 kHz. AE activity is only observed in the discharge phase that combines NBI and ICRH heating, further enhanced if the beams inject T instead of D.

A set of parametric studies are performed dedicated to analyze AE and fish-bone stability in the D–T JET discharge 99896. Three different EP species are analyzed, passing D injected by the NBI, trapped H generated by the ICRH and fusion born alpha particles. The resonance caused by each EP species is studied with respect to the EP density and energy, identifying a bump tail of highly energetic passing D as driver of TAEs and trapped H as driver of fish-bones. The passing D bump tail is generated in the radio-frequency heating scenario that combines NBI and ICRH injection, leading to a population of passing D with energies above 500 keV. On the other hand, the population of alpha particles in the experiment is too small to destabilize AEs. The simulation shows BAEs triggered by alpha particles nearby the magnetic axis if the EP β is more than one order of magnitude higher compared to the experiment observations.

Linear simulations including FLR damping effects identify unstable $3/3-4/3$, $5/4-6/4$ and $7/5-8/5$ TAEs localized at $r/a=0.35$-0.4 with frequencies between 152 and 164 kHz. The $n=4$ TAE shows the largest growth rate. Fish-bones in the frequency range of 25–35 kHz are also identified in the inner plasma region. In addition, marginal unstable RSAE are triggered nearby the magnetic axis in the frequency range of 20–40kHz, mainly damped by the FLR effects. Consequently, linear simulations have reasonable similarities with the observations.

Nonlinear simulations dedicated to study the saturation phase of the TAEs induced by passing D EP show the destabilization of a $4/3-5/3$ TAE in the inner-middle plasma region during the linear phase. The $n=3$ TAE stabilizes along the saturation phase by sharing energy with other modes and thermal plasma, leading to multiple instability signals in low and high frequency ranges as well as the generation of zonal structures. Trapped H EP nonlinear simulation shows the destabilization of fish-bones in the linear phase and overtones with frequencies up to 100 kHz along the saturation phase, caused by the energy transfer towards $n=2$ and 3 toroidal mode families. In addition, the thermal plasma is perturbed due to the fish-bone energy channeling leading to the generation of zonal structures. The saturation of the $1/1$ BAE triggered by alpha particles (hypothetical scenario with EP β one order of magnitude larger than the experiment) shows the destabilization of overtones and the generation of zonal structures.

Transitions from the soft to the hard MHD limit are observed in the nonlinear simulations. For the case of passing D EP simulation, after TAEs stabilize, a global $n=1$ EAE covering main part of the minor radius is triggered leading to a partial collapse of the pressure in the inner plasma region. Strong deformations of the flux surfaces is caused by the large energy transfer from the $n=1$ EAE towards the thermal plasma leading to an enhancement of the zonal structures. It should be recalled that the EAE activity in the experiment is much weaker compared to the simulation, disagreement that could be originated in the intensity of the thermal ion and EP FLR effects as well as the model profiles uncertainty. Hard MHD limit in Trapped H EP and alpha particle simulations is reached once fish-bone or $1/1$ BAE overlap with overtones in the inner plasma, respectively, leading too a partial collapse of the pressure profile due to the large flux surfaces distortion and the enhancement of the zonal structures.

TAE and fish-bone induce a rather weak increment of passing D and trapped H EP transport (below 1% losses) and radial EP redistribution, respectively. These trends are consistent with the almost negligible EP losses measured along the experiment with respect to passing D and trapped H EP once TAEs and fish-bone are destabilized. On the other hand, the hypothetical scenario with unstable $1/1$ BAE triggered by the alpha particles shows 3% losses, further increases to 6% after the hard MHD limit transition. Consequently, the destabilization of BAEs by alpha particles must be avoided because this instability may cause important constrains on the plasma heating efficiency and future devices performance.

Shear flows generation along the saturation phase of TAEs and fish-bones may explain the improvement of the thermal plasma confinement in the discharge. On top of that, TAEs in the inner-middle plasma region induce more intense shear flows with respect to the fish-bone in the inner plasma. The output of the nonlinear simulations also indicates less intense shear flows if TAE and fish-bone activity is weaker, the case of configurations with pure D instead of D–T for the thermal plasma. Indeed, it was observed the thermal plasma confinement improves in D–T experiments compared to pure D plasma, showing a more intense AE/fish-bone activity, explained as a reduction of the plasma turbulence level. That means, shear flows induced by TAE and fish-bones during their saturation phase could be considered as a method to improve the thermal plasma confinement if the EP losses induced are small. Unfortunately, even though passing D and trapped H EP transport is weakly affected by AE/fish-bones, experimental observations indicate significant alpha particles losses [52], research topic explored by simulations with multi ion EP species simulations. Nevertheless, operational scenario of future nuclear fusion reactors may benefit from the presence of shear flows reducing the turbulence transport and the device operation requirements for the L-H transition [121–124]. Indeed, several numerical studies predict a decrease of the plasma turbulence by shear flows induced by AE/EPM [125, 126] and kinetic ballooning modes [127], although it is unclear for other instabilities as interchange modes [128] and tearing modes [68]. In conclusion, the consequences of shear flow generation by AE/fish-bones must be explored in detail for devices as

ITER and JT-60SA, analysis required to understand the impact of these modes saturation on the thermal plasma confinement and the performance of future fusion reactors.

Acknowledgments

The authors would like to thank the JET technical staff for their contributions in the operation and maintenance of JET. We also thanks Alex Tinguely for very productive discussions about TAE-EAE damping rates in JET plasma. This work was supported by the EUROfusion Project CfP-FSD-AWP23-TE-04-JET, the US DOE under Grant DE-FG02-04ER54742, Comunidad de Madrid under the Project 2019-T1/AMB-13648 and the Spanish National Research Project No. PID2022-137869OB-I00. Data available on request from the authors. This work has been carried out within the framework of the EUROfusion Consortium, funded by the European Union via the Euratom Research and Training Programme (Grant Agreement No. 101052200–EUROfusion). Views and opinions expressed are however those of the author(s) only and do not necessarily reflect those of the European Union or the European Commission. Neither the European Union nor the European Commission can be held responsible for them. Use has been made of Uranus, a supercomputed cluster located at the Universidad Carlos III de Madrid (Spain) and funded jointly by EU FEDER funds and by the Spanish Government via national Projects UNC313-4E-23612, ENE2009-12213-C03-03, ENE2012-33219, ENE2012-31753 and ENE2015-68265.

Appendix. Modes saturation and damping effect

This section is dedicated to discuss the effect of the damping included in the linear and nonlinear simulations, as well as the analysis of the saturation times of fish-bones and TAEs in the nonlinear simulations. First, the FLR and electron-ion Landau damping effects are discussed. Next, dedicated nonlinear simulations to characterize the saturation phase of fish-bones and TAE are shown.

A.1. Effect of FLR and electron-ion Landau damping

Linear simulations for trapped H EP driven fish-bones, passing D EP driven TAEs and alpha particle driven BAEs are performed including only the continuum damping effect as well as configurations combining the continuum damping with thermal ion FLR, EP FLR and electron-ion Landau damping effects, respectively. Simulations results are barely affected by the electron-ion Landau damping, corrections in the third decimal of the growth rate and frequency, for all the modes analyzed thus this damping effect is neglected in the linear and nonlinear studies shown in the article. This is not surprising given the rather low thermal electron temperature and thermal ion density in the discharge. Linear simulations with FLR effects assume a thermal and EP Larmor radius of 0.001 and 0.01 m, respectively. The simulations indicate a correction in the second decimal for the fish-bone growth rate and frequency, reason why FLR effects are also neglected for the fish-bone linear and nonlinear studies. This results is also not surprising because low n modes ($n = 1$) with small frequencies (around 25 kHz) and rather wide perturbation width (around $\Delta_{r/a} = 0.3$) should be less impacted by the FLR effects. This approximation reduces the computational cost of the simulation although the destabilization effect of trapped H EP and the fish-bone damping time could be over estimated. On the other hand, FLR damping effects and particularly the EP FLR damping, is essential for the analysis of the TAEs stability. Neglecting the FLR damping leads to the incorrect identification of the dominant modes in the linear and nonlinear simulations compared to the experiment. As it is discussed in the main article text, linear simulations without FLR effects identify EAEs as dominant modes at an incorrect frequency range and radial location with respect to the experimental data, although simulations including the FLR damping shows dominant TAEs at, approximately, the correct frequency range, radial location and mode structure. Again, this is not surprising because high frequency instabilities with slender perturbation radial width triggered by high toroidal mode families must be strongly damped by the FLR effects. Consequently, the linear and nonlinear simulations indicated in the article dedicated to analyze the linear and saturation phase of TAEs include the FLR damping.

A.2. Damping time of fish-bones and TAE

The damping time of fish-bones and TAEs is calculated in the nonlinear simulations and compared with experimental data based on antenna probed stable eigenmodes in JET plasmas [129]. The analysis consists in performing nonlinear simulations removing the EP drive during the linear growth phase of fish-bones and TAEs, calculating the time required by the continuum, FLR and diffusive damping to face away the perturbation.

The first analysis is dedicated to the Fish-bones, recalling the nonlinear simulations are performed neglecting FLR and electron-ion Landau damping, thus only continuum and diffusion damping exist. Figure 26, panel (*a*), indicates the amplitude of the poloidal magnetic field perturbation decreases by one order of magnitude around $100\tau_{A0}$ or 0.049 ms after the EP drive is removed, identified as the fish-bone damping time (t_{damp}). In addition, panels (*b*)–(*e*) show a decrease of the kinetic and magnetic energy of the system by one order of magnitude after $100\tau_{A0}$. Thus, the damping rate can be calculated as $\gamma_{\text{damp}} = t_{\text{damp}}^{-1} = 2.04 \cdot 10^4\ \text{s}^{-1}$. The damping rate normalized with respect to $\omega = 2\pi f$ ($f = 20$ kHz, the frequency of the fish-bone in the simulation) is $\gamma_{\text{damp}}/\omega = 0.16$ (16%). The normalized damping rates measured in DT JET experiments range between 0.06 and 1.0% [129], around ten times smaller compared to the simulations. Nevertheless, the diagnostic can only measure damping rates $< 5\%$, thus the

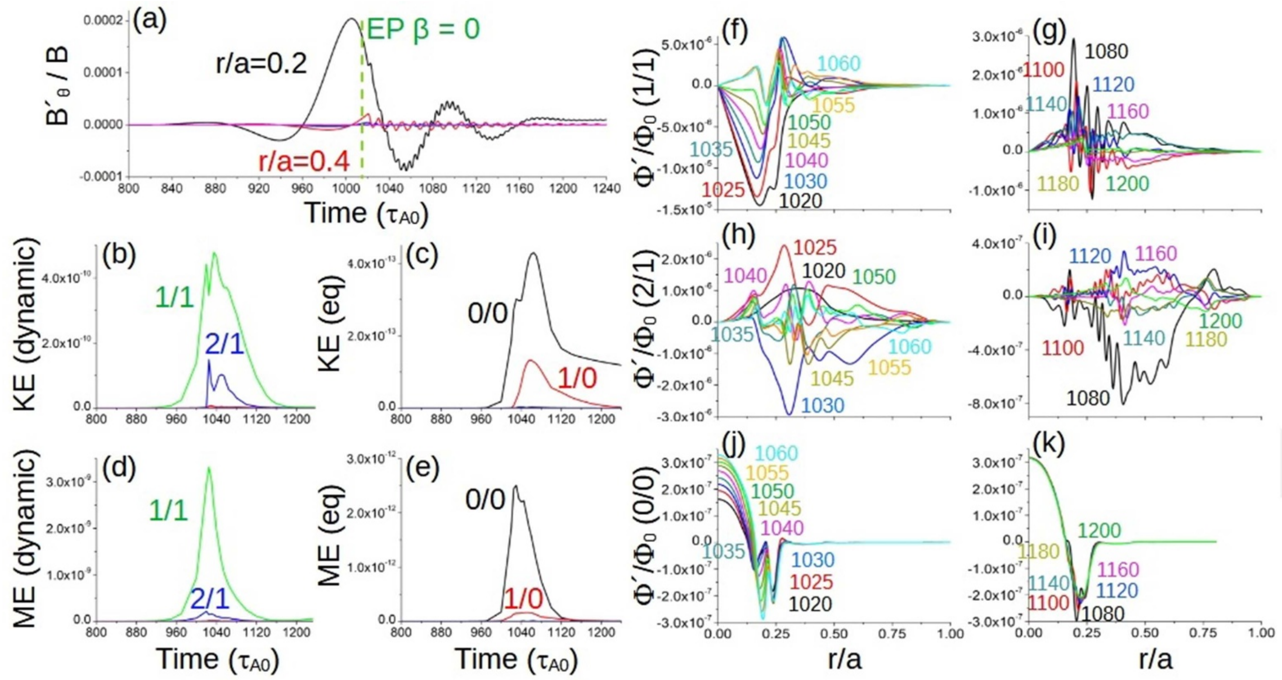

Figure 26. Fish-bone damping analysis. (*a*) Normalized value of the poloidal magnetic field perturbation at different plasma radius ($r/a = 0.2$, black, 0.4, red, 0.6, blue, 0.8, cyan, 1.0, pink). The dashed vertical line indicates the simulation time once EP drive is set to zero ($t = 1020\tau_{A0}$). Volume integrated normalized kinetic energy for (*b*) $n = 1$ to 6 and (*c*) $n = 0$ modes. Volume integrated normalized magnetic energy for (*d*) $n = 1$ to 6 and (*e*) $n = 0$ modes. Evolution of the $1/1$ mode eigenfunction from (*f*) $t = 1020$ to $1100\tau_{A0}$ and (*g*) $t = 1120$ to $1200\tau_{A0}$. Evolution of the $2/1$ mode eigenfunction from (*h*) $t = 1020$ to $1100\tau_{A0}$ and (*i*) $t = 1120$ to $1200\tau_{A0}$. Evolution of the $0/0$ mode eigenfunction from (*j*) $t = 1020$ to $1100\tau_{A0}$ and (*k*) $t = 1120$ to $1200\tau_{A0}$.

damping rate in the simulation is a reasonable estimation. The evolution of $1/1$ mode eigenfunction shows a sharp amplitude decrease as soon as the EP drive stops, reduced by one order of magnitude in $40\tau_{A0}$, panel (*f*). The $1/1$ perturbation maximum localizes around $q = 1$ rational surface showing the amplitude maximum at $t = 1030\tau_{A0}$, approximately half of the amplitude compared to the fish-bone at $t = 1020\tau_{A0}$, pointing out main part of the fish-bone energy is transferred to the continuum. The interaction of the decaying mode with the continuum can be identified in the strong oscillations of the $1/1$ eigenfunction around $q = 1$, panel (*g*). From $t = 1120\tau_{A0}$, $1/1$ eigen-function shows a slender structure localized nearby $q = 1$ (around $r/a = 0.2$) as precursor of $1/1$ internal kink destabilization from $t \approx 1200\tau_{A0}$. A secondary maximum of the $1/1$ eigenfunction is observed in the middle plasma region from $t = 1060\tau_{A0}$ linked to the $q = 2$ rational surface (around $r/a = 0.5$), indicating an energy transfer from the saturating fish-bone towards the $2/1$ perturbation, explain by the toroidal coupling of the poloidal modes of the $n = 1$ toroidal family. Panel (*h*) shows an increment of the $2/1$ eigenfunction amplitude from $t = 1020$ to $1030\tau_{A0}$ up to $1/5$ of the $1/1$ amplitude maximum at $t = 1020\tau_{A0}$, indicating a significant energy transfer from the fish-bones to other coupled poloidal modes of $n = 1$ toroidal family. From $t = 1060\tau_{A0}$, panel (*i*), $2/1$ perturbation maximum displaces to the middle plasma nearby $q = 2$, pointing out the destabilization of the middle plasma region due to the energy transfer from the $1/1$ towards the $2/1$ mode as well as the key role of the energy redistribution between different poloidal modes numbers of the same toroidal mode family during the fish-bone decay. In addition, $0/0$ eigenfunction amplitude increases by a factor two in the inner plasma region, panel (*j*), indicating an enhanced energy channeling from the fish-bone towards the thermal plasma applied to generate zonal structures. The $0/0$ eigenfunction structure remain approximately constant $40\tau_{A0}$ after the EP drive stops, panel (*k*), indicating the energy channeling reaches the steady state very fast consequence of the different time scale ruling the decay of thermal plasma perturbation, resistive times, compared to Alfvenic perturbations. It should be noted the fish-bone destabilization of the thermal plasma promotes the $1/1$ internal kink destabilization after the fish-bone stabilizes.

Next, the TAEs damping rate is calculated applying the same methodology. Figure 27, panel (*a*), indicates the amplitude of the poloidal magnetic field perturbation decreases by 80% around $80\tau_{A0}$ or 0.039 ms after the EP drive is removed, identified as the $n = 3$ TAE damping time. Panels (*b*)–(*e*) also indicate a decrease by 80% of the kinetic and magnetic energy of the system after $80\tau_{A0}$. Thus, $\gamma_{\mathrm{damp}}/\omega = 0.041$ (4.1% for $f = 100$ kHz, the TAE frequency order of magnitude in the simulation). This normalized damping rate is 4 times above the normalized damping rates measure in DT JET experiments, although in the correct range of values considering again the diagnostic can only measure damping rates $< 5\%$. On top of that, discrepancies can exits linked to the Larmor radius of thermal ions and EP assumed in the simulations, leading to a weaker or stronger damping compared to the measured values,

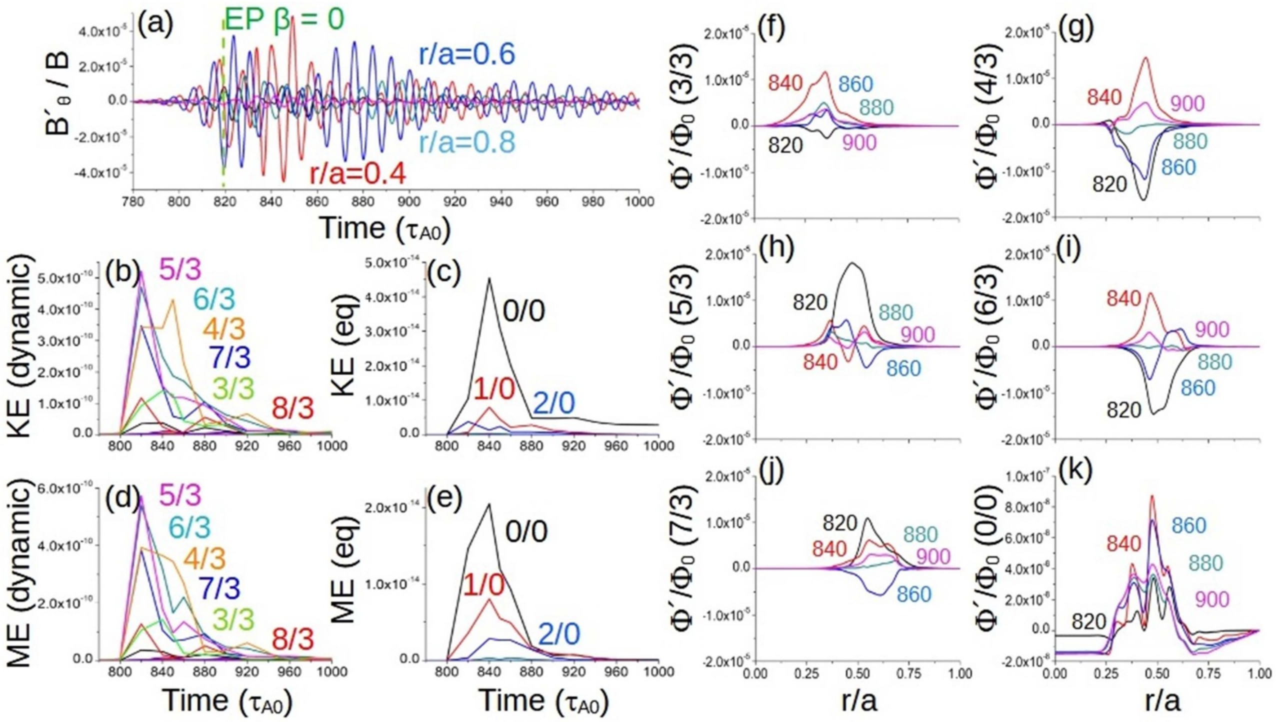

Figure 27. TAE damping analysis. (*a*) Normalized value of the poloidal magnetic field perturbation at different plasma radius ($r/a = 0.2$, black, 0.4, red, 0.6, blue, 0.8, cyan, 1.0, pink). The dashed vertical line indicates the simulation time once EP drive is set to zero ($t = 1020\tau_{A0}$). Volume integrated normalized kinetic energy for (*b*) $n = 1$ to 6 and (*c*) $n = 0$ modes. Volume integrated normalized magnetic energy for (*d*) $n = 1$ to 6 and (*e*) $n = 0$ modes. Evolution of (*f*) $3/3$, (*g*) $4/3$, (*h*) $5/3$, (*i*) $6/3$, (*j*) $7/3$ and (*k*) $0/0$ modes eigenfunction from $t = 820$ to $900\tau_{A0}$.

although the trends identified in the analysis or the study conclusions are not affected. Regarding the evolution of the $4/3 - 5/3$ TAE eigenfunction, the amplitude of the $4/3$ and $5/3$ perturbations, panels (*g*) and (*h*), decreases by 75% $80\tau_{A0}$ after the EP drive stops, showing a smother amplitude reduction compared to the fish-bone case. There is a large coupling and energy sharing between $m = 3$, 6 and 7 poloidal modes of $n = 3$ toroidal family as can be observed in panels (*f*), (*i*) and (*j*) respectively, pointing out the important role of the toroidal mode couplings in TAEs saturation could even more important compared to the fish-bone case. Energy channeling towards the thermal plasma is also observed following the evolution of the $0/0$ perturbation, panel (*k*).

References

[1] Appel L.C. *et al* 1995 *Nucl. Fusion* **35** 1697
[2] Todo Y. *et al* 2019 *Rev. Mod. Plasma Phys.* **3** 1
[3] Heidbrink W.W. and White R.B. 2020 *Phys. Plasmas* **27** 030901
[4] Bass E.M. and Waltz R.E. 2020 *Nucl. Fusion* **60** 016032
[5] Ogawa K. *et al* 2022 *Nucl. Fusion* **62** 112001
[6] McGuire K.M. *et al* 1995 *Phys. Plasmas* **2** 2176
[7] Fitzgerald M. *et al* 2023 *Nucl. Fusion* **63** 112006
[8] Fu G.Y. *et al* 1995 *Phys. Rev. Lett.* **75** 2336
[9] Shinohara K. *et al* 2001 *Nucl. Fusion* **41** 603
[10] Garcia-Munoz M. *et al* 2011 *Nucl. Fusion* **51** 103013
[11] Van Zeeland M.A. *et al* 2019 *Nucl. Fusion* **59** 086028
[12] Hole M.J., Qu Z.S., Layden B., Michael C.A., Woo M.H., Bak J.G., Kim J. and Hezaveh H. 2019 *Plasma Phys. Control. Fusion* **61** 025016
[13] Xu L. *et al* 2021 *Nucl. Fusion* **61** 076005
[14] Weller A., Spong D.A., Jaenicke R., Lazaros A., Penningsfeld F.P. and Sattler S. 1994 *Phys. Rev. Lett.* **72** 1220
[15] Ogawa K., Isobe M., Toi K., Watanabe F., Spong D.A., Shimizu A., Osakabe M., Ohdachi S. and Sakakibara S. 2010 *Nucl. Fusion* **50** 084005
[16] Slaby C. *et al* 2020 *Nucl. Fusion* **60** 112004
[17] Yamamoto S. *et al* 2020 *Nucl. Fusion* **60** 066018
[18] Cappa A. *et al* 2021 *Nucl. Fusion* **61** 066019
[19] D'Ippolito D.A. *et al* 1980 *Plasma Phys.* **22** 1091
[20] van der Holst B., Beliën A.J.C. and Goedbloed J.P. 2000 *Phys. Rev. Lett.* **84** 2865
[21] Ido T. *et al* 2015 *Nucl. Fusion* **55** 083024
[22] Wang H., Todo Y., Ido T. and Suzuki Y. 2018 *Phys. Rev. Lett.* **120** 175001
[23] Sharapov S.E. *et al* 2013 *Nucl. Fusion* **53** 104022
[24] Tinguely R.A. *et al* 2022 *Nucl. Fusion* **62** 112008
[25] Kiptily V.G. *et al* 2022 *Plasma Phys. Control. Fusion* **64** 064001
[26] Teplukhina A.A. *et al* 2023 *Plasma Phys. Control. Fusion* **65** 035023
[27] Sharapov S.E. *et al* 2023 *Nucl. Fusion* **63** 112007
[28] Oliver H.J.C. *et al* 2023 *Nucl. Fusion* **63** 112008

[29] Ali-Arshad S. and Campbell D.J. 1995 *Plasma Phys. Control. Fusion* **37** 715
[30] Fitzgerald M. *et al* 2022 *Nucl. Fusion* **62** 106001
[31] Heidbrink W.W., Fasoli A., Borba D. and Jaun A. 1997 *Phys. Plasmas* **4** 3663
[32] Ahlgren T., Sharapov S.E., Breizman B.N. and Zheng L.-J. 2017 *Phys. Plasmas* **24** 122505
[33] Sharapov S.E. *et al* 2002 *Phys. Plasmas* **9** 2027
[34] Nabais F. *et al* 2005 *Phys. Plasmas* **12** 102509
[35] Borba D. *et al* 2002 *Nucl. Fusion* **42** 1029
[36] Testa D., Spong D., Panis T., Blanchard P. and Fasoli A. 2011 *Nucl. Fusion* **51** 043009
[37] Aslanyan V. *et al* 2019 *Nucl. Fusion* **59** 026008
[38] Mazzi S., Garcia J., Zarzoso D., Kazakov Y.O., Ongena J., Dreval M., Nocente M., Štancar ž and Szepesi G. 2022 *Plasma Phys. Control. Fusion* **64** 114001
[39] Chen L. and Zonca F. 2012 *Phys. Rev. Lett.* **109** 145002
[40] Qiu Z., Chen L. and Zonca F. 2017 *Nucl. Fusion* **57** 056017
[41] Spong D., Van Zeeland M.A., Heidbrink W.W., Du X., Varela J., Garcia L. and Ghai Y. 2021 *Nucl. Fusion* **61** 116061
[42] Ge W., Wang Z.-X., Wang F., Liu Z. and Xu L. 2023 *Nucl. Fusion* **63** 016007
[43] Varela J. *et al* 2023 *Plasma Phys. Control. Fusion* **65** 125004
[44] Shen W., Fu G.Y., Tobias B., Van Zeeland M., Wang F. and Sheng Z.-M. 2015 *Phys. Plasmas* **22** 042510
[45] Shen W., Wang F., Fu G.Y., Xu L. and Ren Z. 2020 *Nucl. Fusion* **60** 106016
[46] Brochard G. *et al* 2024 *Phys. Rev. Lett.* **132** 075101
[47] Han X. *et al* 2022 *Nucl. Fusion* **62** 064005
[48] Varela J. *et al* 2025 *Nucl. Fusion* **65** 026002
[49] Maggi C.F. *et al* 2024 *Nucl. Fusion* **64** 112012
[50] Mailloux J. *et al* 2022 *Nucl. Fusion* **62** 042026
[51] Garcia J. *et al* 2023 *Nucl. Fusion* **63** 112003
[52] Garcia J. *et al* 2024 *Nat. Commun.* **15** 7846
[53] Duesing G., Altmann H., Falter H., Goede A., Haange R., Hemsworth R.S., Kupschus P., Stork D. and Thompson E. 1987 *Fusion Sci. Technol.* **11** 163
[54] Ciric D. *et al* 2011 *Fusion Sci. Technol.* **86** 509
[55] Bhatnagar V.P., Jacquinto J., Start D.F.H. and Tubbing B.J.D. 1993 *Nucl. Fusion* **33** 83
[56] Start D.F.H. *et al* 1999 *Nucl. Fusion* **39** 321
[57] Kazakov Y.O., Van Eester D., Dumont R. and Ongena J. 2015 *Nucl. Fusion* **55** 032001
[58] Kazakov Y.O. *et al* 2017 *Nat. Phys.* **13** 973
[59] Kazakov Y.O. *et al* 2020 *Nucl. Fusion* **60** 112013
[60] Nocente M. *et al* 2020 *Nucl. Fusion* **60** 124006
[61] Spong D.A., Carreras B.A. and Hedrick C.L. 1994 *Phys. Plasmas* **1** 1503
[62] Spong D.A. *et al* 2014 *Plasma Fusion Res.* **9** 3403077
[63] Hedrick C.L., Leboeuf J.-N. and Spong D.A. 1992 *Phys. Fluids B* **4** 3869
[64] Varela J. , Spong D., Garcia L., Ghai Y. and Ortiz J. 2024 *Front. Phys.* **12** 1
[65] Hirshman S.P. , Whitson J.C. 1983 *Phys. Fluids* **26** 3553
[66] Sauter O. *et al* 1997 *Phys. Plasmas* **4** 1654
[67] Buttery R.J. *et al* 2000 *Plasma Phys. Control. Fusion* **42** B61
[68] Wang Z.-X., Wang X., Dong J.Q., Kishimoto Y. and Li J.Q. 2008 *Phys. Plasmas* **15** 082109
[69] Garcia L., Carreras B.A., Dominguez N., Leboeuf J.N. and Lynch V.E. 1990 *Phys. Fluids B* **2** 2162
[70] Hammett G.W. , Perkins F.W. 1990 *Phys. Rev. Lett.* **64** 3019
[71] Spong D.A. *et al* 2013 *Nucl. Fusion* **53** 053008
[72] Varela J. *et al* 2020 *Nucl. Fusion* **60** 096009
[73] Taimourzadeh S. *et al* 2019 *Nucl. Fusion* **59** 066006
[74] Varela J., Spong D.A. and Garcia L. 2017 *Nucl. Fusion* **57** 046018
[75] Varela J., Spong D.A., Garcia L., Ohdachi S., Watanabe K.Y. and Seki R. 2019 *Nucl. Fusion* **59** 046008
[76] Varela J., Ohdachi S., Watanabe K.Y., Spong D.A., Garcia L. and Seki R. 2020 *Nucl. Fusion* **60** 046013
[77] Osakabe M. *et al* 2022 *Nucl. Fusion* **62** 042019
[78] Varela J. *et al* 2024 *Phys. Plasmas* **31** 082504
[79] Pace D.C. *et al* 2018 *Phys. Plasmas* **25** 056109
[80] Varela J. *et al* 2018 *Nucl. Fusion* **58** 076017
[81] Varela J., Spong D.A., Murakami M., Garcia L., D'Azevedo E., Van Zeeland M.A. and Munaretto S. 2019 *Nucl. Fusion* **59** 046017
[82] Huang J. *et al* 2020 *Nucl. Fusion* **60** 126007
[83] Ghai Y., Spong D.A., Varela J., Garcia L., Van Zeeland M.A. and Austin M.E. 2021 *Nucl. Fusion* **61** 126020
[84] Varela J., Spong D.A. and Garcia L. 2017 *Nucl. Fusion* **57** 126019
[85] Eliseev L. *et al* 2021 *Phys. Plasma* **28** 072510
[86] Hidalgo C. *et al* 2022 *Nucl. Fusion* **62** 042025
[87] Varela J. *et al* 2020 *Nucl. Fusion* **60** 112015
[88] Varela J. *et al* 2023 *Nucl. Fusion* **63** 026009
[89] Varela J., Garcia L., Ohdachi S., Watanabe K.Y. and Sanchez R. 2012 *Phys. Plasmas* **19** 082501
[90] Varela J., Watanabe K.Y. and Ohdachi S. 2012 *Phys. Plasmas* **19** 082512
[91] Varela J., Watanabe K.Y., Ohdachi S. and Narushima Y. 2014 *Phys. Plasmas* **21** 032501
[92] Varela J., Watanabe K.Y., Ohdachi S. and Narushima Y. 2014 *Phys. Plasmas* **21** 092505
[93] Varela J., Spong D.A., Garcia L., Todo Y., Huang J. and Murakami M. 2019 *Phys. Plasmas* **26** 062502
[94] Varela J., Spong D.A. and Garcia L. 2019 *Nucl. Fusion* **59** 076036
[95] Varela J., Huang J., Spong D.A., Chen J., Chan V., Garcia L., Wingen A., Ghai Y. and Zou Y. 2022 *Nucl. Fusion* **62** 036005
[96] Varela J., Shimizu A., Spong D.A., Garcia L. and Ghai Y. 2021 *Nucl. Fusion* **61** 026023
[97] Ortiz J., Varela J., Spong D.A., Garcia L. and Ghai Y. 2023 *Nucl. Fusion* **63** 056010
[98] Varela J., Spong D.A., Garcia L., Ohdachi S., Watanabe K.Y., Seki R. and Ghai Y. 2021 *Nucl. Fusion* **61** 126016
[99] Varela J., Spong D.A., Todo Y., Garcia L., Ghai Y., Ortiz J. and Seki R. 2022 *Nucl. Fusion* **62** 126020
[100] Ongena J., Voitsekhovitch I., Evrard M. and McCune D. 2012 *Fusion Sci. Technol.* **61** 180
[101] Pankin A., McCune D., Andre R., Bateman G. and Kritz A. 2004 *Comput. Phys. Commun.* **159** 157
[102] Brambilla M. *et al* 1999 *Plasma Phys. Control. Fusion* **41** 1
[103] Grierson B.A. *et al* 2018 *Fusion Sci. Technol.* **74** 101
[104] Pasqualotto R., Nielsen P., Gowers C., Beurskens M., Kempenaars M., Carlstrom T. and Johnson D. 2004 *Rev. Sci. Instrum.* **75** 3891
[105] Noterdaeme J.-M. *et al* 2003 *Nucl. Fusion* **43** 274
[106] Brix M., Hawkes N.C., Boboc A., Drozdov V. and Sharapov S.E. 2008 *Rev. Sci. Instrum.* **79** 10F325
[107] Maggi C.F. *et al* 2017 *Nucl. Fusion* **60** 014045
[108] Nabais F. *et al* 2022 *Nucl. Fusion* **62** 104001
[109] Brizard A.J. *et al* 2011 *Phys. Plasmas* **18** 022508
[110] Spong D.A., Sanchez R. and Weller A. 2003 *Phys. Plasmas* **10** 3217
[111] Gorelenkov N.N. *et al* 2007 *Plasma Phys. Control. Fusion* **49** B371
[112] Silva C., Hillesheim J.C., Hidalgo C., Belonohy E., Delabie E., Gil L., Maggi C.F., Meneses L., Solano E. and Tsalas M. 2016 *Nucl. Fusion* **56** 106026
[113] Pucella G. *et al* 2022 *Plasma Phys. Control. Fusion* **64** 045023
[114] Citrin J. *et al* 2013 *Phys. Rev. Lett.* **111** 155001
[115] Doerk H., Bock A., Di Siena A., Fable E., Görler T., Jenko F. and Stober J. 2018 *Nucl. Fusion* **58** 016044

[116] Todo Y., Berk H.L. and Breizman B.N. 2010 *Nucl. Fusion* **50** 084016
[117] Todo Y., Berk H.L. and Breizman B.N. 2012 *Nucl. Fusion* **52** 094018
[118] Falchetto G.L. and Ottaviani M. 2004 *Phys. Rev. Lett.* **92** 025002
[119] Whelan G.G., Pueschel M.J., Terry P.W., Citrin J., McKinney I.J., Guttenfelder W. and Doerk H. 2019 *Phys. Plasmas* **26** 082302
[120] Xu J.Q. *et al* 2022 *Phys. Plasmas* **29** 012508
[121] Burrell K.H. *et al* 1999 *Phys. Plasmas* **6** 4418
[122] Schmitz L. 2017 *Nucl. Fusion* **57** 025003
[123] Burrell K.H. *et al* 2020 *Phys. Plasmas* **27** 060501
[124] Mazzi S. *et al* 2022 *Nucl. Fusion* **62** 096024
[125] Di Siena A. *et al* 2019 *Nucl. Fusion* **59** 124001
[126] Ishizawa A., Imadera K., Nakamura Y. and Kishimoto Y. 2021 *Nucl. Fusion* **61** 114002
[127] McKinney I., Pueschel M.J., Faber B.J., Hegna C.C., Ishizawa A. and Terry P.W. 2021 *J. Plasma Phys.* **87** 905870311
[128] Li B., Sun C.K., Wang X.Y., Zhou A., Wang X.G. and Ernst D.R. 2015 *Phys. Plasmas* **22** 112304
[129] Tinguely R.A. *et al* 2022 *Nucl. Fusion* **62** 076001